

Chemical distribution of HII regions towards the Galactic anticentre

A. Fernández-Martín^{1,2} *, E. Pérez-Montero¹, J.M. Vílchez¹, and A. Mampaso^{3,4}.

¹ Instituto de Astrofísica de Andalucía (IAA-CSIC), Glorieta de la Astronomía S/N, 18008 Granada, Spain

² Instituto de Radioastronomía y Astrofísica (IRyA-UNAM), 58089 Morelia, Mexico

³ Instituto de Astrofísica de Canarias (IAC), 38200 La Laguna, Tenerife, Spain

⁴ Departamento de Astrofísica, Universidad de La Laguna, 38206 La Laguna, Tenerife, Spain

Preprint online version: April 29, 2022

ABSTRACT

Context. The study of the radial variations of metallicity across the Galactic disc is a powerful method for understanding the history of star formation and chemical evolution of the Milky Way. Although several studies about gradients have been performed so far, the knowledge of the Galactic anticentre is still poor.

Aims. This work aims to determine accurately the physical and chemical properties of a sample of H II regions located at $R_G > 11$ kpc and to study the radial distribution of abundances in the outermost part of the Galaxy disc.

Methods. We carried out new optical spectroscopic observations of nine H II regions with the William Herschel Telescope covering the spectral range from 3500 Å to 10100 Å. In addition, we increased the sample by searching the literature for optical observations of regions towards the Galactic anticentre, re-analysing them to obtain a single sample of 23 objects to be processed in a homogeneous and consistent manner. The total sample distribution covers the Galactocentric radius from 11 kpc to 18 kpc.

Results. Emission line ratios were used to determine accurate electron densities and temperatures of several ionic species in 13 H II regions. These physical parameters were applied to the spectra to determine direct total chemical abundances. For those regions without direct estimations of temperature, chemical abundances were derived by performing tailor-made photoionisation models and/or by using an empirical relation obtained from radio recombination and optical temperatures.

We performed weighted least-squares fits to the distribution of the derived abundances along the Galactocentric distances to study the radial gradients of metallicity across the outermost part of the MW. The distributions O/H, N/H, S/H, and Ar/H towards the anticentre can be represented by decreasing linear radial gradients, while in the case of N/O abundances the radial distribution is better fitted with a two-zone model. The He/H radial gradient is presented here for the first time; we find a slope that is not significantly different from zero. The derived gradient for oxygen shows a clear decrease with distance with a slope of -0.053 ± 0.009 dex kpc⁻¹. Although a shallower slope at large Galactocentric distances is suggested by our data, the flattening of the distribution cannot be confirmed and more objects towards the anticentre need to be studied in order to establish the true form of the metallicity gradient.

Key words. ISM: abundances – HII regions – Galaxy: abundances – Galaxy: disc – Galaxy: evolution

1. Introduction

The chemical evolution of the interstellar medium (ISM) varies between galaxies and is both position and time dependent within a galaxy. Since the nucleosynthesis of different elements occurs in stars of different masses, the study of chemical abundances in the discs of spiral galaxies is a powerful method for understanding the history of star formation and evolution of galaxies.

A knowledge of the radial variations of metallicity across the galactic disc (i.e. abundance gradients) is central to our understanding of a wide variety of observed phenomena, including the physics of star formation rates (Phillipps & Edmunds 1991), initial mass function (Guesten & Mezger 1982), the radial inflows/outflows of gas (Mayor & Vigroux 1981), and the stellar evolution and the process of nucleosynthesis itself. Galactic abundance gradients in the ISM were first described by Searle (1971) in a survey of H II regions in six late-type spiral galaxies. Since then, considerable effort has been made to establish the chemical distribution in the Milky Way (MW) by studying many sources such as supernova remnants (SNR) (Binette et al. 1982), molecular clouds (Rudolph et al. 1996), open clusters (Twarog et al. 1997; Andreuzzi et al. 2011), cepheids (Luck et al. 2003; Korotin et al. 2014), OB stars (Rolleston et al.

2000), and planetary nebulae (PNe) (Maciel & Koppen 1994; Henry et al. 2010). However, when deriving the abundances representative of the current ISM values, H II regions provide the most accessible probe of abundances gradients. Since they are bright and hot they emit strongly in many lines observable over much of the MW. Unlike stars, H II regions probe the current state of abundances, and unlike PNe and SNR, do not contaminate the surrounding ISM.

The existence of a large-scale gradient in the MW with H II regions was established by the pioneering work of Shaver et al. (1983), who found a decrease of metallicity with Galactic distances. Subsequently, several studies with H II regions (Hawley 1978; Talent & Dufour 1979; Fich & Silkey 1991; Hunter 1992; Afflerbach et al. 1997; Vílchez & Esteban 1996; Deharveng et al. 2000; Rudolph et al. 2006) have been carried out, firmly establishing the existence of a negative gradient of abundance of the elements heavier than helium in the disc of the MW.

Nonetheless, the sampling of the whole Galactic disc is still poor. In particular, relatively few H II regions have been studied towards the Galactic anticentre region. Optically, there are only ten Galactic H II regions which have been observed at $R_G > 11$ kpc and for which direct measurements of the electron temperature are available. This is also a handicap for the MW stud-

* e-mail: alba@iaa.es

Table 1. Names and positions of the H II regions observed with WHT-ISIS and log of observations.

H II region ^(a)	α_{J2000} (h m s)	δ_{J2000} ($^{\circ}$ $'$ $''$)	Airmass ^(b)	Exp. Time ^(c) (s)	Date
S83	19:24:30.77	+20:47:45.92	1.18	3×1800	July, 13, 2010
S132	22:19:08.26	+56:05:12.98	1.37	3×1800	July, 13, 2010
S156	23:05:08.33	+60:14:46.29	1.23	3×700 / 3×200 ^(d)	July, 13, 2010
S162	23:20:43.94	+61:12:27.06	1.20	500+900+1000 / 18×100 ^(d,e)	July, 13, 2010
S207	4:19:49.49	+53:09:34.91	1.27	3×1200	Dec., 19, 2009
S208	4:19:32.39	+52:58:38.98	1.21	3×1500	Dec., 19, 2009
S212	4:40:36.50	+50:27:44.31	1.14	3×1500	Dec., 19, 2009
S228	5:13:23.37	+37:27:19.63	1.02	3×1500	Dec., 19, 2009
S270	6:10:12.96	+12:48:37.38	1.24	1200+1300+1500 ^(e)	Dec., 19, 2009

^(a) Sh2-number is the IAU standard notation for objects in Sharpless (1959) catalogue. For consistence with other works and simplification, in this paper we identify them as S-number.

^(b) Mean value during the observations.

^(c) In all the regions, except S156 and S162, the blue and red arms were acquired simultaneously with the same exposition time.

^(d) Individual times for each grating are indicated for S156 and S162 separated by a bar (blue/red).

^(e) Regions S162 and S270 were observed with different exposition times (with the same arm). This was taking into account when combining images in the data reduction.

ies, compared with those for nearby external galaxies, and limits the application of models of galactic evolution. In particular, it limits those aspect of the models that describe the evolution of the outermost parts of the disc, which might be considered – at least from the point of view of the chemical evolution – to be much closer to the pre-galactic/early conditions in the MW. Moreover, the possibility of variations in the slope of the gradients in the outer disc has been a subject of debate in the past years. Some authors have claimed that radial abundance gradients of some elements may flatten out at the outer parts of the Galactic disc (Fich & Silkey 1991; Vílchez & Esteban 1996), while other authors do not support such flattening (Deharveng et al. 2000; Rudolph et al. 2006).

Therefore, extending the measurement of abundances to large Galactocentric distances in the MW is essential to our understanding of the metallicity gradient and the chemical evolution of our Galaxy.

This paper has two main purposes. The first is to present new long-slit observations in a wide spectral range of H II regions located towards the Galactic anticentre with Galactocentric distances from 11 kpc to 17 kpc. The second is to present a re-determination of chemical abundances, from direct electron temperatures and from physical modelling, of all the optical outermost H II regions observations in the literature in a homogeneous and consistent manner to perform a self-consistent study of the chemical gradients towards the outermost disc of the MW. The wide optical spectral range covered, together with the consistent chemical analysis of the sample, allowed us to give an accurate description of the radial chemical distribution towards the Galactic anticentre up to a distance of 18 kpc.

In the following section we present the data sample including our own observations and other data from the literature. Section 3 describes the analysis and the results of the study, while Sect. 4 is devoted to discussing the resulting abundance gradients and their implications in the context of Galactic evolution. Finally, we describe the main conclusions of this work in Sect. 5.

2. Sample of H II regions

This work aims to study the chemical abundances of H II regions located towards the Galactic anticentre. Therefore we selected Galactic H II regions in the direction of the anticentre with $R_G > 11$ kpc from catalogues of Fich & Blitz (1984), Deharveng et al. (2000), and Quireza et al. (2006). The mother sample includes 89 anticentre H II regions observable from the northern hemisphere.

2.1. Selection and observations of WHT data

We selected for our observations those H II regions from the mother sample located at the furthest distance from the Galactic centre and, if possible, with available information on their thermal structure (e.g. a radio continuum temperature). Nine H II regions located at $11 \text{ kpc} < R_G < 17 \text{ kpc}$ were observed; their names and positions are listed in Table 1.

The observations were carried out in December 2009 and July 2010 using the ISIS double-armed spectrograph at the 4.2 m William Herschel Telescope (WHT) at the Observatorio del Roque de los Muchachos (La Palma, Spain). A dichroic was set at $\sim 5336 \text{ \AA}$ permitting simultaneous observation in the blue and red arms, which are optimised for their respective wavelength ranges. The blue arm detector, EEV12, is an array of 4096×2048 ($13.5 \mu\text{m}$) pixels giving a spatial resolution of 0.2 arcsec/pix , while the CCD for the ISIS red arm, RED+, is a red-sensitive array of 4096×2048 ($15.0 \mu\text{m}$) with a spatial resolution of 0.22 arcsec/pix . The gratings were chosen in order to obtain as much information as possible on the most important emission lines of the optical range. In the blue arm, the R300B grating was centred at 4400 \AA covering the effective spectral range from 3200 \AA to 5800 \AA with a dispersion of 0.86 \AA/pix , giving a spectral resolution of $R = \lambda/\delta\lambda \sim 1070$ at 4400 \AA . In the red arm, the R158R was centred at 7800 \AA covering the effective spectral range from 5300 \AA to 10000 \AA with a dispersion of 1.81 \AA/pix and a spectral resolution of $R \sim 1010$ at 7800 \AA .

Table 1 also shows the observational log for the H II regions of the observed sample. At least three exposures were taken

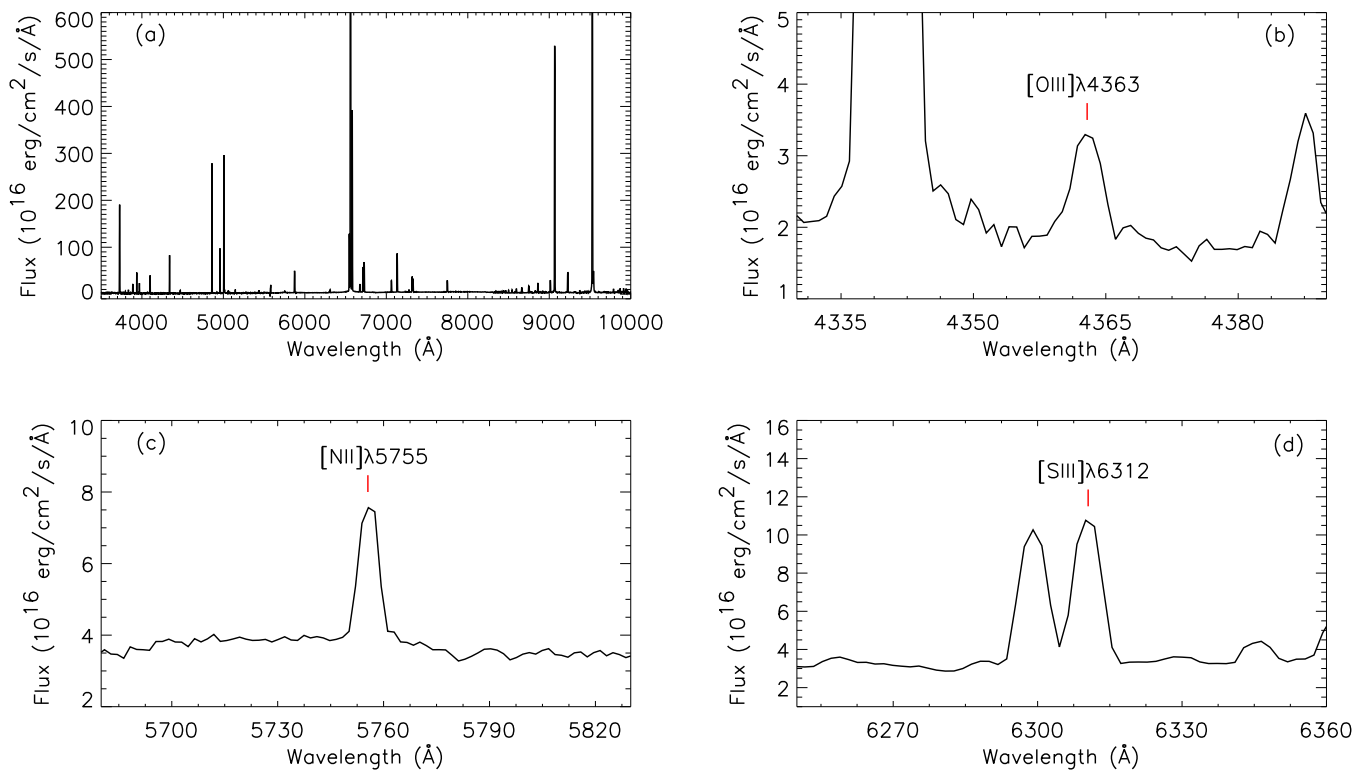


Fig. 1. Extracted observed flux-calibrated spectra. From left to right and top to bottom: (a) whole integrated spectrum of S156, (b) subset of the spectrum of S162 showing the temperature sensitive line [O III] λ 4363, (c) subset of the spectrum of S162 showing the temperature sensitive line [N II] λ 5755, and (d) subset of the spectrum of S162 showing the temperature sensitive line [S III] λ 6312.

in each region with different exposition times depending on the object. The slit width was set at 1 arcsec throughout the observation and oriented in parallactic angle to avoid differential atmospheric refraction problems. The necessary bias frames, continuum, arcs, and spectrophotometric standard stars were also acquired.

The spectra were reduced using IRAF¹ by following the standard procedure for 2D spectroscopic observations (bias subtraction, flat-fielding, and cosmic ray rejection). The wavelength calibration was made using CuNe+CuAr arcs taken shortly after the object spectrum was taken. Two spectrophotometric standard stars were observed each night (G191-B2B and HR345 in December 2009, and BD+26 2603 and BD+17 4708 in July 2010) so that the spectra could be flux calibrated.

For each exposure, a background region was selected in order to avoid nebular emission or stars. Pixels of these regions were combined with a median in a single spectrum and a 2D background spectrum was created with the value of the combined spectrum in each column. This sky background was subsequently subtracted from every science object. This method was used in all the H II regions except for S162 where the S156-sky was used for the sky subtraction since S162 was too extended and no area without nebular emission was found. The sky subtraction worked well overall; only the strongest sky-lines in the far red spectra ($\lambda > 9000$ Å) left some residuals.

¹ The Image Reduction and Analysis Facility IRAF is distributed by the National Optical Astronomy Observatories, which are operated by the Association of Universities for Research in Astronomy, Inc., under cooperative agreement with the National Science Foundation.

In order to select the zones to extract the 1D spectra we examined the spatial profiles of the most important emission lines, whenever possible selecting areas with emission of the auroral lines necessary to estimate the electron temperature. The spectra were traced and extracted using the APALL task in IRAF with an aperture optimised for a good S/N which was able to minimise the contamination of adjacent pixels; in this process we took into account the different spatial scales between blue and red arms. Eighteen spectra were finally extracted over the sample. In Fig. 1 we present four representative examples showing the auroral lines necessary to estimate electron temperatures.

2.2. Additional data from the literature

To realise a more extensive study of the Galactic anticentre, the sample was increased with H II regions from previous works. With this aim, we carried out an exhaustive bibliographical review, selecting those H II regions located at $R_G > 11$ kpc observed in the optical range and with measurements of the electron temperature sensitive lines or, at least, with information about the [S III] λ 9068 line to obtain chemical abundances by means of individual photoionization models.

As a result of this search we found 14 H II regions that satisfy the stipulated requirements: S98, S127, S128, S209, S219, S266 (B), S283, and S203 (BFS31) from Vílchez & Esteban (1996); S255 (c), S301 (RCW6), and S311 (RCW16a) from Shaver et al. (1983); S158 (P1) from Talent & Dufour (1979); S206 from Caplan et al. (2000); and S298 (B2) from Esteban et al. (1990). Some authors provide information about regions in several pointings; in these cases we chose those with more

emission lines measured (in parentheses we indicate the pointing selected for our study and the identification given by each author).

2.3. Final sample

The final sample to be analysed in this work includes both samples described above (Sects. 2.1 and 2.2) and consists of 23 H II regions located in a range of Galactocentric distances from 11 kpc to 18 kpc. In Table 2 we present a summary of the fundamental physical parameters of the H II regions analysed in this study. Each H II region is identified in Col. 1 by its Sharpless number (Sharpless 1959). Columns 2 and 3 give the Galactic coordinates (l,b). Columns 4 and 5 give the Galactocentric and heliocentric distances (R_G and d_\odot), both of which are analysed and justified in Sect. 4.1. Column 6 shows the distance above the Galactic plane (z), and Col. 7 gives the angular size of the nebula (Θ). In Col. 9 we show the spectral type of the dominant exciting star. Column 10 gives the electron temperature derived from radio observations (t_e^*) and, finally, Col. 11 indicates other identification names. The corresponding references are given in the footnotes.

3. Analysis and results

3.1. Line intensities and reddening correction

We now report on the method used to obtain the line intensities of the regions observed with ISIS (our own sample). Line fluxes were measured by integrating all the flux in the line between two given limits and over a fitted local continuum. Partially blended lines, such H α and [N II] $\lambda\lambda$ 6548,6584, were deblended with two or three Gaussian profiles to measure the individual line fluxes. All the measurement were made with the SPLOT task of IRAF. The statistical errors associated with the observed fluxes were calculated using the expression

$$\sigma_1 = \sigma_c N^{1/2} [1 + EW/(N\Delta)]^{1/2}, \quad (1)$$

where σ_1 represents the error in the observed line flux, N is the number of pixels used to measure the line, EW the line equivalent width, σ_c the standard deviation of the continuum in a box near the line, and Δ represents the dispersion in $\text{\AA}/\text{pix}$ (Pérez-Montero & Díaz 2003).

The reddening coefficient $c(H\beta)$ was derived from the observed flux ratios of the brightest Balmer lines H α /H β , H γ /H β , and H δ /H β as compared with the theoretical values obtained from the public software of Storey & Hummer (1995) assuming Case B recombination and following an iterative process with the n_e and t_e estimations (Sect. 3.2). To minimise the reddening effect and to avoid error propagation due to differences between red and blue grating calibrations, the measured lines were reddening corrected relative to H β , H α , or P10 (if S/N>5) depending on the spectral range and later normalised to H β flux using the corresponding theoretical ratios.

Table 3 lists the reddening-corrected intensities of the emission lines measured for every observed H II region labelled with their standard identification. The third column gives the adopted reddening function, $f(\lambda)$, using the extinction law by Cardelli et al. (1989) with $R_V = 3.1$. Errors in the emission line intensities were derived by propagating the observational errors in the fluxes and the reddening constant uncertainties. The estimated fluxes and errors were normalised to $F(H\beta)=1000$. The values obtained for $c(H\beta)$ are also presented in the last row of Table 3.

At zero redshift the [S III] λ 9530 \AA line fluxes are strongly affected by a sky absorption band. Therefore, this line was not used for the derivation of the [S III] electron temperature neither for the S^{++}/H^+ ionic abundance. For these quantities a theoretical ratio [S III] λ 9530/[S III] λ 9069=2.44 was assumed.

The methodology used to obtain the intensities of the H II regions selected from the literature was different since in these regions we did not measure the fluxes in spectra. In this case, we calculated the original reddened fluxes considering the extinction law and $c(H\beta)$ used by each author and later we re-derived the intensities following the same self-consistent method as in our regions: theoretical Balmer lines with Case B recombination, iterative process with n_e and t_e , and reddening function using the extinction law by Cardelli et al. (1989) with $R_V = 3.1$. Finally, we obtained consistent intensities derived exactly under the same conditions as in our sample. Data from these 14 H II regions were added to our new observations reported here to create a data set of 23 H II regions with $11 \text{ kpc} < R_G < 18 \text{ kpc}$. Hereafter we work with all of these objects as a single sample following the same methodology for both samples.

3.2. Physical parameters

To obtain the physical conditions of the gas, we performed an iterative process for each region until an agreement was achieved between electron density (n_e) and electron temperature (t_e). The values for t_e and n_e derived for each H II region are shown in Table 4. Those regions without measurements of auroral lines necessary to estimate at least one electron temperature were discarded temporarily. Physical parameters and chemical abundances were not derived with this direct method for any of them and, therefore, they are not included in Table 4 (but see Sects. 3.4 and 3.5).

Electron density, n_e , was calculated for all the observed regions from the [S II] $\lambda\lambda$ 6717,6731 line ratio using the IRAF package TEMDEN based on a five-level statistical equilibrium model (De Robertis et al. 1987; Shaw & Dufour 1995). Electron temperatures, t_e , were derived using the appropriate line ratios R_{N2} , R_{O3} , R_{S3} , R_{O2} , and R'_{S2} following the equations below for each ion:

$$t_e([N \text{ II}]) = 0.537 + 0.000253 R_{N2} + 42.126/R_{N2}; \quad (2)$$

$$t_e([O \text{ III}]) = 0.8254 - 0.0002415 R_{O3} + 47.77/R_{O3}; \quad (3)$$

$$t_e([S \text{ III}]) = [R_{S3} + 36.4] / [1.8 R_{S3} - 3.01]; \quad (4)$$

$$t_e([O \text{ II}]) = a_0(n_e) + a_1(n_e) R_{O2} + a_2(n_e)/R_{O2},$$

where $a_0(n_e) = 0.23 - 0.005 n_e - 0.17/n_e$
 $a_1(n_e) = 0.007 + 0.000009 n_e + 0.0064/n_e$
 $a_2(n_e) = 38.3 - 0.021 n_e - 1.64/n_e;$ (5)

$$t_e([S \text{ II}]) = a_0(n_e) + a_1(n_e) R'_{S2} + a_2(n_e)/R'_{S2} + a_3(n_e)/R'^2_{S2},$$

where $a_0(n_e) = 1.92 - 0.0017 n_e + 0.848/n_e$
 $a_1(n_e) = -0.0375 + 4.038 \cdot 10^{-5} n_e - 0.0185/n_e$
 $a_2(n_e) = -14.15 + 0.019 n_e - 10.4/n_e$
 $a_3(n_e) = 105.64 + 0.019 n_e + 58.52/n_e.$ (6)

In all the equations, electron density is in units of cm^{-3} and electron temperatures in units of 10^4 K .

Table 2. Fundamental physical parameter of the H II regions. Numbers indicate the corresponding references (see footnote and text for details).

Region	l ($^{\circ}$)	b ^[1] ($^{\circ}$)	R _G (kpc)	d ₀ (kpc)	z ^[7] (pc)	Θ ^[1] (arcsec)	Spectral type of dominant exciting star	t _e [*] ($\times 10^4$ K)	Other names
S83	55.12	2.42	15.2 ^[2]	18.7 ^[2]	-	2	-	-	-
S98	68.15	1.02	12.8 ^[3]	13.3 ^[3]	-	15	O4V ^[8]	1.08 ^[3]	-
S127	96.29	2.60	13.9 ^[2]	12.2 ^[2]	698	2	O8V ^[9]	1.14 ^[3]	-
S128	97.50	3.16	12.7 ^[2]	9.0 ^[2]	484	1	O7V ^[9]	1.04 ^[3]	-
S132	102.79	-0.65	11.3 ^[4]	5.8 ^[4]	-59	90	O8.5V ^[13] /B0III ^[14] /WN6 ^[15]	-	-
S156	110.11	0.06	11.5 ^[4]	5.3 ^[4]	6	2	O8V ^[10] /O6.5V ^[15] /O7V ^[16]	0.92 ^[3] /0.91 ^[4]	-
S158	111.55	0.82	12.4 ^[4]	6.4 ^[4]	38	10	O9V ^[10]	0.85 ^[3] /0.82 ^[4]	NGC7538
S162	112.22	0.23	11.1 ^[4]	4.7 ^[4]	13	40	O7I ^[9] /O6.5III ^f ^[11,16]	0.86 ^[3] /0.81 ^[4]	NGC7635
S203	143.81	-1.57	11.3 ^[5]	3.3 ^[5]	-	2	B2V ^[10]	-	BFS31
S206	150.58	-0.94	11.1 ^[2]	2.8 ^[2]	-44	50	O4 ^[15] /O5V ^[16] /O5neb ^[17]	1.00 ^[3] /0.97 ^[4]	-
S207	151.19	2.13	16.8 ^[2]	4.3 ^[2]	-	4	O9V ^[12,13] /O9.5IV ^[9,17]	-	-
S208	151.31	1.99	16.8 ^[2]	4.1 ^[2]	261	1	O9.5V ^[9] /B0V ^[12,17]	-	-
S209	151.60	-0.25	16.9 ^[4]	8.9 ^[4]	-51	14	O9III ^[9]	1.08 ^[3] /1.05 ^[4]	-
S212	155.35	2.60	16.7 ^[4]	8.6 ^[4]	278	5	O6I ^[9] /O7f ^[15] /O5.5neb ^[17]	1.03 ^[3] /1.05 ^[4]	-
S219	159.36	2.60	13.3 ^[2]	4.5 ^[2]	189	3	B2.5V ^[10] /B0V ^[16,17]	-	-
S228	169.21	-0.90	13.8 ^[4]	5.3 ^[4]	-	8	O8Ve ^[9,13] /B0V ^[15]	0.94 ^[3] /0.97 ^[4]	-
S255	192.64	0.00	11.0 ^[5]	2.5 ^[5]	-2	3	B0V ^[15] /B0III ^{neb} ^[17]	-	-
S266	195.66	-0.09	17.9 ^[6]	9.6 ^[6]	-15	1	BeI? ^[18]	-	-
S270	196.83	-3.10	14.2 ^[6]	5.9 ^[6]	-478	1	-	-	-
S283	210.81	-2.56	17.0 ^[6]	9.1 ^[6]	-407	3	B3V ^[10] /O7V ^[10] /B1V ^[10] /B0:V ^[17]	-	-
S298	227.75	-0.15	12.4 ^[4]	5.0 ^[4]	-7	22	WN5 ^[14,17]	1.25 ^[3] /1.36 ^[4]	NGC2359/RCW5
S301	231.45	-4.41	12.9 ^[4]	5.8 ^[4]	-439	9	O6V ^[16] /O7 ^[17] /B1III ^[17]	0.91 ^[3] /0.97 ^[4]	RCW6
S311	243.16	0.36	12.0 ^[4]	5.4 ^[4]	32	45	O5V ^[13] /O6.5V ^[13] /O6 ^[14]	1.05 ^[3] /1.02 ^[4]	RCW16

References: [1]=Blitz et al. (1982), [2]=Caplan et al. (2000), [3]=Balser et al. (2011), [4]=Quiroza et al. (2006), [5]=Rudolph et al. (2006), [6]=Fich & Silkey (1991), [7]=Fich & Blitz (1984), [8]=Mampaso (1991), [9]=Chini & Wink (1984), [10]=Russeil et al. (2007), [11]=Conti & Leep (1974), [12]=Crampton et al. (1978), [13]=Crampton & Fisher (1974), [14]=Georgelin & Georgelin (1970), [15]=Hunter & Massey (1990), [16]=Georgelin et al. (1975), [17]=Moffat et al. (1979), [18]=Vilchez & Esteban (1996).

Table 4. Electron densities and electron temperatures.

H II region	n _e (cm ⁻³)	t _e ([N II]) (10 ⁴ K)	t _e ([O III]) (10 ⁴ K)	t _e ([S III]) (10 ⁴ K)	t _e ([O II]) (10 ⁴ K)	t _e ([S II]) (10 ⁴ K)
S83	256 ± 62	1.16 ± 0.03 _E	1.14 ± 0.05	1.13 ± 0.02	-	-
S127	325 ± 75	-	1.01 ± 0.13 _E	0.88 ± 0.15 _E	0.91 ± 0.05	-
S128	<100	-	0.92 ± 0.15 _E	0.77 ± 0.18 _E	0.98 ± 0.12	-
S132	315 ± 15	0.96 ± 0.05	0.82 ± 0.07 _E	0.81 ± 0.02	-	0.84 ± 0.09
S156	1133 ± 29	0.96 ± 0.04	0.92 ± 0.03	0.80 ± 0.01	-	0.87 ± 0.18
S158	1323 ± 265	0.99 ± 0.15	0.87 ± 0.21 _E	0.72 ± 0.25 _E †	-	-
S162	1440 ± 23	0.93 ± 0.03	0.94 ± 0.02	0.80 ± 0.03	-	0.81 ± 0.03
S206	357 ± 161	-	0.95 ± 0.02	-	0.87 ± 0.05 _E	-
S212	211 ± 29	1.11 ± 0.06	1.21 ± 0.04	1.18 ± 0.03	-	-
S255	321	0.82	0.65 _E	-	-	-
S298	<100	-	1.20 ± 0.03	1.11 ± 0.04 _E	1.17 ± 0.08 _E	-
S301	<100	-	<0.91	<0.77 _E	<0.96 _E	-
S311	130	0.95	0.87	0.72 _E	-	0.88

_E Electron temperatures derived from other t_e (see text for details).

† In region S158 t_e([S III]) has S/N<3. This fact was taken into account when deriving abundances.

Our criterion in the determination of the electron temperature was to derive at least one temperature characteristic for each ionisation degree: t_e([O III]) as the high-ionisation zone, t_e([S III]) as the medium-ionisation zone, and t_e([N II]), t_e([S II]), or t_e([O II]) as the low-ionisation zone. However, not all the necessary auro-

ral lines were detected in all the regions (we did not estimate t_e for all the ions). For S206, S298, and S301 no auroral line asso-

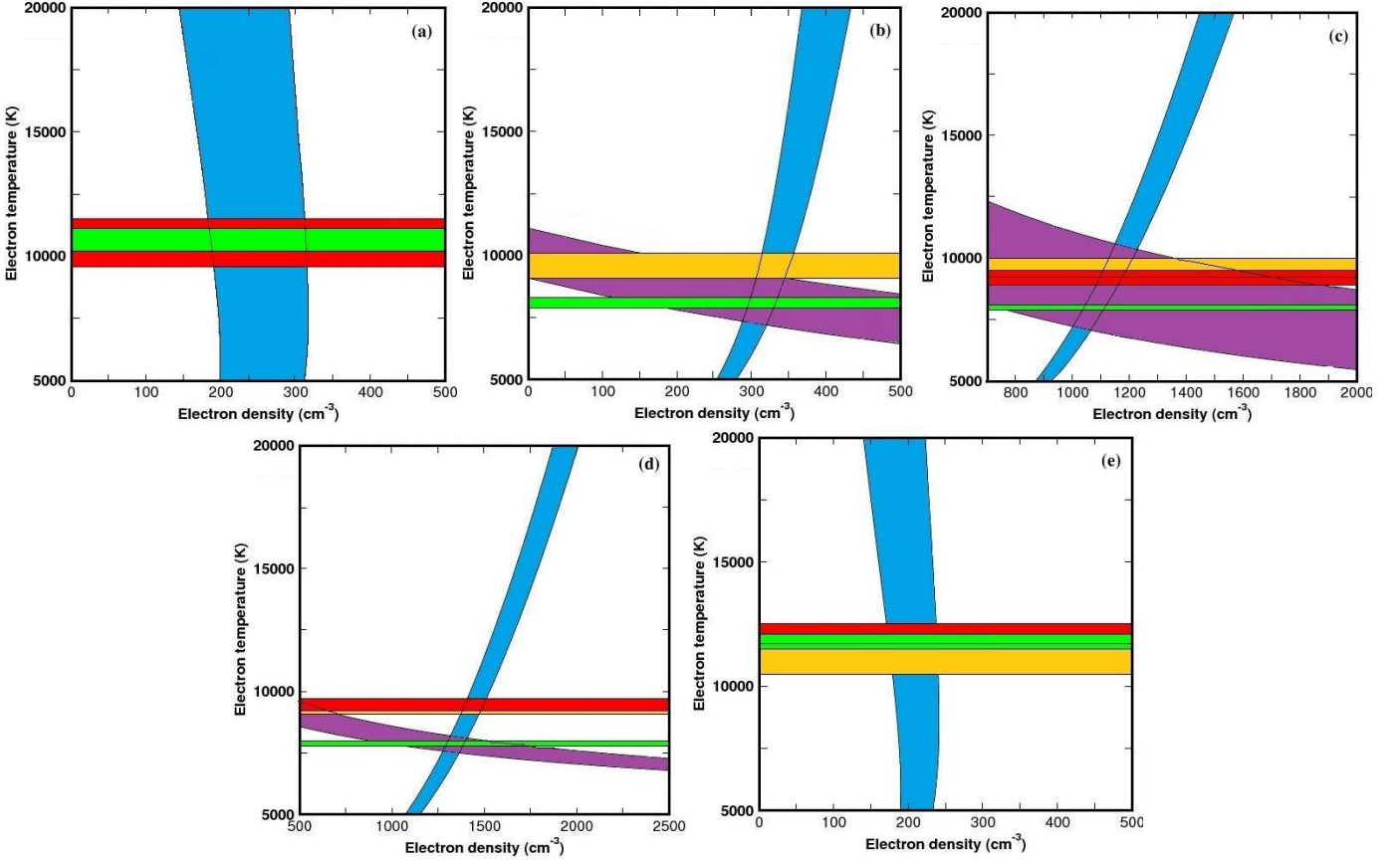


Fig. 2. T_e - n_e diagnostic diagrams of H II regions observed with ISIS with direct electron temperatures estimations: (a) S83, (b) S132, (c) S156, (d) S162, and (e) S212. Blue bands correspond to n_e , purple to t_e ([S II]), yellow to t_e ([N II]), red to t_e ([O III]), and green to t_e ([S III]).

ciated with a low-excitation ion was observed and we resorted to the expression

$$t_e([\text{O II}]) = \frac{1.2 + 0.002 n_e + 4.2/n_e}{t_e([\text{O III}])^{-1} + 0.08 + 0.003 n_e + 2.5/n_e}, \quad (7)$$

which relates $t_e([\text{O II}])$ with $t_e([\text{O III}])$ (Pérez-Montero & Contini 2009). Equation 7 was also used for S127 and S128, in which we inferred $t_e([\text{O III}])$ from $t_e([\text{O II}])$. In the case of S132, S158, and S255 we estimated $t_e([\text{O III}])$ by using the relation

$$t_e([\text{O III}]) = \frac{t_e([\text{N II}])}{1.85 - 0.72 t_e([\text{N II}])} \quad (8)$$

obtained from Pérez-Montero & Contini (2009). A similar scenario occurs when deriving t_e ([S III]) in regions in which [S III] λ 6312 and [S III] λ 9068,9530 were not measured simultaneously (S127, S128, S158, S298, S301, and S311). For these objects we resorted to the expression proposed by Pérez-Montero & Díaz (2003) that relates t_e ([S III]) with t_e ([O III]):

$$t_e([\text{S III}]) = 1.19 t_e([\text{O III}]) - 0.32. \quad (9)$$

Equations 7 and 8 are based on photoionisation models, while equation 9 was obtained with observational data. Electron temperatures estimated with these methods are quoted in Table 4 labelled with the subscript E.

Although the intensities of the necessary auroral lines are relatively reliable, the estimation of the electron temperature is not exempt from problems. There are several sources of

uncertainty that need to be mentioned because the variations in the temperature would involve offsets in the chemical abundances. Kennicutt et al. (2003) compare the consistency of electron temperatures measured from different ions based on observation of H II regions in M101. They find that the temperatures derived from the [O II] λ 7325 line show a large scatter and are nearly uncorrelated with temperatures derived from other ions. The source of this disagreement remains unresolved, but they speculate on possible sources such as dielectronic recombination, collisional de-excitation, radiative transfer effects, and observational uncertainties. On the other hand, Binette et al. (2012) analyse pairs of [O II] and [S II] temperatures in H II regions finding that T_e ([O III]) appears to be higher than T_e ([S III]) in objects with T_e ([S III]) lower than 14000 K. They perform photoionisation models to look for an explanation for this trend and conclude that models with metallicity inhomogeneities or with shock waves that propagate in the photoionised gas successfully reproduce the observed excess in T_e ([O III]) temperatures.

In order to determine the uncertainties in physical parameters and to analyse possible discrepancies between electron temperatures associated with different ions, we performed diagnostic diagrams that show t_e dependences with n_e and vice versa. We represented extreme values of t_e and n_e characterised by the flux ratios and their observational errors obtaining diagnostic bands that allow us to visualise the electron temperature structure in the ionised gas.

Figure 2 shows the diagnostic diagrams generated for the WHT regions with direct estimation of t_e : S83, S132, S156, S162, and S212. We show the electron density and its dependence with t_e in blue. Yellow, red, and green bands represent electron temperatures independent of density, respectively $t_e(\text{N II})$, $t_e(\text{O III})$, and $t_e(\text{S III})$. Finally, we represent the single electron temperature sensitive to density, $t_e(\text{S II})$, in purple. The criterion used to paint the parameters is arbitrary and the parameters are represented giving preference to some of them following this order: $t_e(\text{S III})$ - $t_e(\text{O III})$ - $t_e(\text{N II})$ - $t_e(\text{S II})$ - n_e . For this reason, in some regions certain temperatures are not clearly observed because they are hidden behind others.

Analysing the density variations, we found that S83, S132, and S212 always show medium densities with values between 150 cm^{-3} and 400 cm^{-3} , while S156 and S162 present higher densities with a wider range of values, from 800 cm^{-3} to 2000 cm^{-3} , for a given temperature. In general, the agreement between electron temperatures is very good, and it is possible to appreciate the consistency both for t_e ranges of different ions at estimated n_e and for values presented in Table 4. The electron temperature associated with [S III] is the only one that shows lower values than the others in three regions for a fixed density; this has been taken into account for the derivation of ionic abundances, as we show in the next section.

3.3. Direct chemical abundances

The ionic chemical abundances of the different species were estimated from the forbidden-to-hydrogen emission line ratios of the strongest available emission lines detected in the analysed spectra. We resorted to the functional forms given by Hägele et al. (2008) which are based on the package IONIC of IRAF. To determine the single ionised helium abundance we used the equations proposed by Olive & Skillman (2004). We checked that results for He^+/H^+ with this method do not differ more than ~ 3 per cent from values estimated with recent emissivities proposed by Porter et al. (2013). We also calculated the mean weighted by the errors of the five observed He I lines ($\text{He I } \lambda 4026$, $\text{He I } \lambda 4471$, $\text{He I } \lambda 5875$, $\text{He I } \lambda 6678$, and $\text{He I } \lambda 7065$). The ionic abundances of the different elements with respect to ionised hydrogen along with their corresponding errors are given in Table 5.

To estimate the chemical abundances, electron density and temperature were required. We derived each ionic abundance with its corresponding electron temperature, if it was possible. In this way we estimated O^+ with $t_e(\text{O II})$, O^{2+} with $t_e(\text{O III})$, S^+ with $t_e(\text{S II})$, S^{2+} with $t_e(\text{S III})$, and N^+ with $t_e(\text{N II})$. In the case of argon we assumed $t_e(\text{Ar III})=t_e(\text{S III})$ (Garnett 1992), while for iron, helium, and neon the ionic abundances were derived under the assumption that $t_e(\text{Fe III})=t_e(\text{O III})$, $t_e(\text{He I})=t_e(\text{O III})$, and $t_e(\text{Ne III})=t_e(\text{O III})$ (Peimbert & Costero 1969). For those regions where not all the electron temperatures were derived we assumed an ionisation structure: the adopted criterion was to derive abundances with electron temperatures related with ions with the same excitation degree and similar ionisation potential. Nonetheless, we must bear in mind that assuming that temperatures are uniform in a given ionisation zone, our results can be subject to slight changes if we consider the presence of temperature inhomogeneities (Esteban et al. 2009; Mesa-Delgado & Esteban 2010; Stasińska et al. 2013). The temperature fluctuation paradigm was proposed by Peimbert (1967) and it is characterised by the mean square of the spatial distribution of temperature (the so-called temperature fluctuation parameter t^2). Our direct chemical abundances are derived using the standard method based on

collisional excited lines (CELs), which have a strong dependence on T_e ; therefore, temperature fluctuations can result in an underestimation of the absolute abundances of the ionised gas. This will be considered in the analysis of the chemical gradients.

The total abundances were derived by taking into account, when required, the unseen ionisation stages of each element, using the appropriate ionisation correction factor (ICF) for each species. The O/H was obtained by directly adding the two ionic abundances ($\text{O}/\text{H} \sim \text{O}^+/\text{H}^+ + \text{O}^{2+}/\text{H}^+$). The N/O can be approximated to N^+/O^+ and the N/H ratio as $\text{N}/\text{H} \sim (\text{N}/\text{O}) \times (\text{O}/\text{H})$. Due to the spectral range of our observations, no [S IV] line was observed, but – by taking the excitation condition into account – a relatively important contribution from S^{3+} may be expected in these H II regions. Therefore, the total sulfur abundance was inferred using the $\text{ICF}(\text{S}^+ + \text{S}^{2+})$ proposed by Barker (1980). The total abundances of neon and argon were calculated using the ionisation correction factors $\text{ICF}(\text{Ne}^{2+})$ and $\text{ICF}(\text{Ar}^{2+})$, respectively, given by Pérez-Montero et al. (2007). The total abundance of iron was inferred using the $\text{ICF}(\text{Fe}^{2+})$ proposed by Rodríguez & Rubin (2004). Finally, in the case of helium we do not detect the $\text{He II } \lambda 4686$ line (belonging to the observed spectral range) in any region and we can assume that $\text{He}^{2+}=0$. On the other hand, it is expected that the contribution of the unobservable neutral helium was important. In this work, we adopted the $\text{ICF}(\text{He}^+ + \text{He}^0)$ proposed by Peimbert et al. (1992) to consider the He^0 contribution. In Table 5 we present the total direct abundances and the ICFs derived along with their corresponding errors.

3.4. Tailor-made photoionisation models

For those regions without a detection of any auroral temperature-sensitive emission line (e.g. [N II] $\lambda 5755$, [O III] $\lambda 4363$) we were not able to derive chemical abundances following the direct method. Instead, it is possible to apply methods based on strong emission line ratios, such as R_{23} , O_3N_2 , or S_{23} . However, most of these methods have been calibrated for massive star-forming complexes whose scales and properties do not match those in our sample of nebulae ionised by single stars in the disc of the Galaxy. As an alternative, we can resort to tailor-made photoionisation models covering the observed properties of these objects.

In Table 2 we showed the spectral type of the dominant exciting stars of the sample. These spectral types were derived by different authors using different methods, and great discrepancies among authors in spectral types for the same star are found. For this reason, and in order to work with a self-consistent sample, we decided to estimate representative effective temperatures resorting to the η' parameter instead of that derived from the spectral type in Table 2.

The spectral energy distributions (SEDs) of the ionising stars can be obtained from the observed emission line ratios using appropriate diagnostic diagrams that yield a stellar effective temperature. This is the case of the η parameter (Vilchez & Pagel 1988), defined as

$$\eta = \frac{\text{O}^+/\text{O}^{2+}}{\text{S}^+/\text{S}^{2+}}, \quad (10)$$

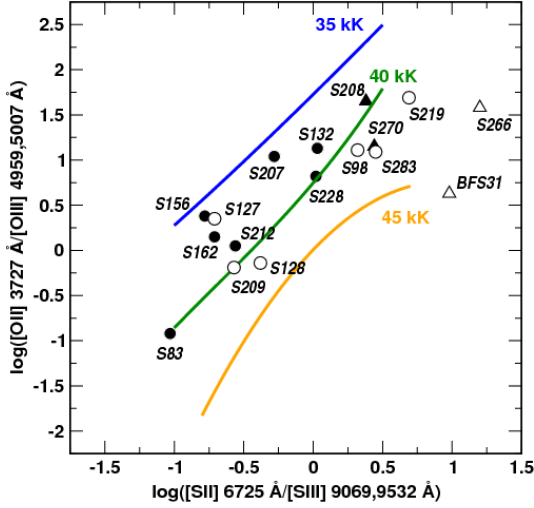


Fig. 3. $[S II]/[S III]$ versus $[O II]/[O III]$ in logarithm units compared with a grid of WM-Basic models at $Z=0.2 Z_{\odot}$. The solid lines represent models with the same effective temperature as indicated. Circles show H II regions with reliable line emission measurements and triangles regions with upper limit intensities. Filled symbols represent data from our own sample (observed regions) while open symbols represent regions taken from the literature.

which is sensitive to the hardness of the ionising spectral energy distribution. When the ionic abundances cannot be derived, it is possible to use the η' parameter based on emission lines:

$$\eta' = \frac{[O II]_{3727} / [O III]_{4959, 5007}}{[S II]_{6717, 6731} / [S III]_{9069, 9532}}. \quad (11)$$

Although this parameter mainly correlates with the stellar effective temperature, it also has an additional dependence on electron temperature and, hence, on chemical abundance. We then used the calibration of the η' parameter presented by Pérez-Montero et al. (2014) based on fittings to models with WM-Basic (Pauldrach et al. 2001) single stars at a metallicity $Z=0.2 Z_{\odot}$ close to the expected values for this subsample. The η' criterion limits the use of models when deriving chemical abundances to those H II regions with the four involved emission lines. All the H II regions with measures of $[O II]_{\lambda 3727}$, $[O III]_{\lambda 5007}$, $[S II]_{\lambda 6717, 6731}$, and $[S III]_{\lambda 9069}$ are shown along with the models used to derive the effective temperature in Fig. 3.

Once the ionising SEDs were established, we used the photoionisation code Cloudy v13.03 (Ferland et al. 2013) using as input conditions a constant density in the gas according to the value derived from the ratio of $[S II]$ emission lines and a dust-to-gas ratio with a standard value of 2×10^{-3} . All models have a radiation-bounded geometry and the stopping criterion is that 99% of the H atoms are ionised. The models for each region are repeated in an iterative process varying $Q(H)$, the inner radius, the number of hydrogen ionising photons, the abundance of all elements scaled to oxygen, and the nitrogen-to-oxygen ratio that most closely reproduces the observed $[O II]_{\lambda 3727}/H\beta$, $[O III]_{\lambda 5007}/H\beta$, $[N II]_{\lambda 6584}/[O II]_{\lambda 3727}$, and the $H\beta$ luminosity. In the S208, S219, S266, and S270 regions, the $[O III]_{\lambda 5007}$ line is not detected or it has a very weak flux, so we considered an upper limit of this line two times the uncertainty associated with the continuum at the same wavelength. The typical number of it-

Table 6. Obtained properties from the resulting tailor-made photoionisation models.

	T_{eff} (kK)	$\log L(H\beta)$ (erg/s)	Radius (pc)	$12+\log(O/H)$	$\log(N/O)$
S83*	40	34.15	0.1	8.16	-0.95
S98	41	35.02	4.4	8.16	-1.06
S127*	37	34.33	0.3	8.29	-1.34
S128*	41	34.57	0.7	8.21	-1.00
S132*	38	33.02	0.1	8.32	-0.98
S156*	36	34.11	0.1	8.26	-0.95
S162*	37	33.57	3.0	8.30	-0.86
S207	40	34.23	2.0	8.13	-1.06
S208	39	33.90	1.7	>8.31	<-0.96
S212*	39	34.76	4.1	8.15	-1.06
S219	42	33.35	3.7	>7.92	<-0.86
S228	40	34.33	1.4	8.23	-0.92
S266	42	33.21	0.6	>8.11	<-0.78
S270	42	34.53	1.1	>7.72	<-0.66
S283	42	33.17	1.0	8.20	-1.19

* H II regions with chemical abundances also estimated with the direct method.

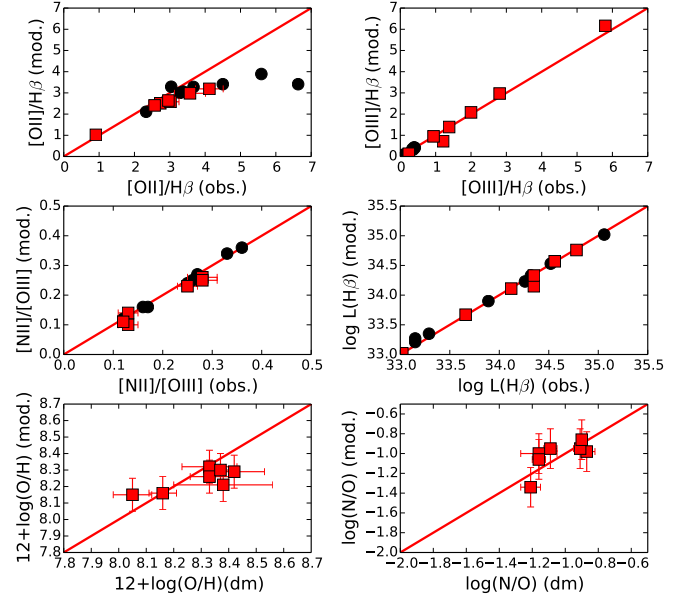


Fig. 4. Upper and middle rows show a comparison between observed quantities and the found solutions of the tailor-made models, while in the last row we compare the chemical abundances obtained from models with those derived with the direct method. Red squares represent H II regions with direct estimations of T_e and black circles represent regions without a detection of any auroral temperature-sensitive emission line.

erations before a solution is found is around 50, with the exception of S203 and S209 where no reliable solutions were found. In the former region, the relatively very high $[O III]/H\beta$ ratios is possibly due to a density-bounded geometry and in the latter to possible aperture effects.

The obtained properties from the resulting models, including $L(H\beta)$, external radius, oxygen abundance, and N/O ratios are summarised in Table 6. Figure 4 shows the agreement between the four observed quantities and the found solutions. With the exception of $[O II]/H\beta$ in S98 and S283, errors in the accuracy of

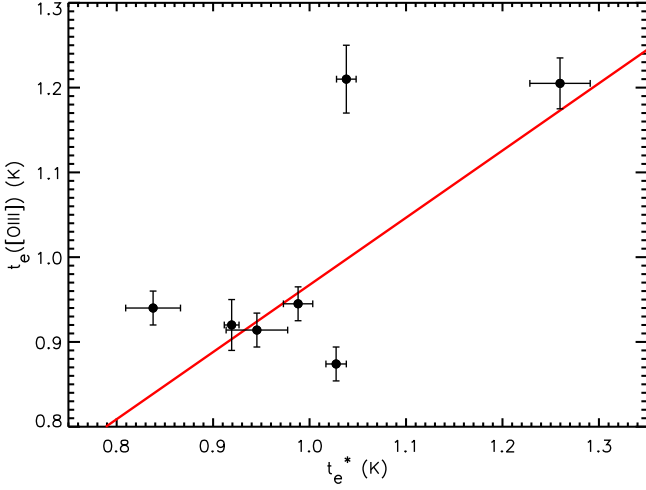


Fig. 5. Comparison of optical electron temperatures derived from the [O III] lines, $t_e([\text{O III}])$, with those derived from the radio recombination lines, t_e^* . The red solid line represents the fit performed weighted by errors.

the adjustments are less than 1 per cent for $H\beta$ luminosity, 5 per cent for $[\text{O III}]/H\beta$ and $[\text{N II}]/[\text{O II}]$, and 10 per cent for $[\text{O II}]/H\beta$. In S98 and S283 the observed very high value of $[\text{O II}]/H\beta$ is possibly due to some contamination from the diffuse gas. In the last row of Fig. 4 we also show the comparison between chemical abundances obtained from models (Table 6) with those derived with the direct method (Table 5). As can be seen, the results from the two methods are in good agreement showing that the two treatments are consistent.

3.5. Relation between radio and optical electron temperatures

In this subsection we perform a comparative analysis of the optical and radio electron temperatures to derive a relation between them. Since there is a large sample of nebulae widely distributed across the Galactic disc with estimations of electron temperatures based on radio recombination lines (RRL) and continuum data, this relation could be used to obtain the optical temperature and to calculate chemical abundances in those cases without detectable optical auroral lines.

Most of the observed emission lines in ionised nebulae are collisionally excited and their intensities depend exponentially on temperature. This temperature can be determined from appropriate line ratios. However, these ratios involve the detection and measurement of auroral lines which are intrinsically weak and remain undetected in many objects. On the other hand, most of the radio emission observed from H II regions is continuum radiation produced by free-free thermal bremsstrahlung in the plasma. At high frequencies the nebular gas is optically thin, and the ratio between the brightness temperature of a RRL and that of a free-free emission continuum depends on the radio frequency and the gas temperature. Thus, the observed RRL-to-continuum ratio can be used to estimate the electron temperature of the H II regions (Rohlf & Wilson 2000). Because the RRLs are not obscured by interstellar dust, relatively faint H II regions at large distances from the Sun can be detected, allowing radio electron temperatures t_e^* to be estimated more easily than with optical auroral lines.

Table 7. Electron temperatures, electron densities, and ionic and total chemical abundances obtained from the t_e - t_e^* relation.

	S98	S209	S228
t_e^* (10^4 K)	1.08 ± 0.02	1.06 ± 0.01	0.94 ± 0.01
$t_e([\text{O III}])$ (10^4 K)	1.03 ± 0.12	1.02 ± 0.12	0.92 ± 0.11
$t_e([\text{N II}])$ (10^4 K)	1.10 ± 0.07	1.09 ± 0.07	1.02 ± 0.07
$t_e([\text{S III}])$ (10^4 K)	0.91 ± 0.14	0.89 ± 0.14	0.78 ± 0.13
n_e (cm^{-3})	<100	423 ± 49	233 ± 12
$12+\log(\text{O}^+/\text{H}^+)$	8.23 ± 0.12	7.84 ± 0.12	8.13 ± 0.13
$12+\log(\text{O}^{2+}/\text{H}^+)$	7.06 ± 0.21	7.94 ± 0.17	7.27 ± 0.19
$12+\log(\text{S}^+/\text{H}^+)$	5.94 ± 0.08	5.47 ± 0.08	6.07 ± 0.07
$12+\log(\text{S}^{2+}/\text{H}^+)$	6.14 ± 0.18	6.43 ± 0.17	6.51 ± 0.18
$12+\log(\text{N}^+/\text{H}^+)$	7.21 ± 0.08	6.70 ± 0.08	7.26 ± 0.08
$\log(\text{N}^+/\text{O}^+)$	-1.01 ± 0.07	-1.10 ± 0.08	-0.85 ± 0.06
(He ⁺ /H ⁺) 5875	-	0.08 ± 0.01	-
(He ⁺ /H ⁺) 6678	-	0.08 ± 0.03	0.09 ± 0.01
(He ⁺ /H ⁺) 7065	-	0.07 ± 0.02	0.07 ± 0.01
(He ⁺ /H ⁺)	-	0.08 ± 0.01	0.08 ± 0.01
ICF(S ⁺ , S ²⁺)	1.00 ± 0.01	1.11 ± 0.07	1.00 ± 0.01
ICF(He ⁺)	-	1.10 ± 0.04	1.36 ± 0.16
$12+\log(\text{O}/\text{H})$	8.26 ± 0.12	8.19 ± 0.11	8.18 ± 0.12
$12+\log(\text{S}/\text{H})$	6.36 ± 0.12	6.52 ± 0.16	6.65 ± 0.13
$12+\log(\text{N}/\text{H})$	7.24 ± 0.19	7.05 ± 0.19	7.29 ± 0.19
$\log(\text{N}/\text{O})$	-1.01 ± 0.07	-1.10 ± 0.08	-0.85 ± 0.06
He/H	-	0.09 ± 0.01	0.11 ± 0.02

With the intention of establishing a relation to convert t_e^* into optical electron temperatures t_e which are relevant in abundance determinations, we first checked the literature for studies with reliable estimations of radio temperatures (see Col. 9 of Table 2). Later, we compared these values with our optical electron temperatures derived from the [O III] lines (see Col. 4 of Table 4) for H II regions in common. Figure 5 shows optical electron temperatures, $t_e([\text{O III}])$, derived in this work as a function of the radio temperatures, t_e^* , adopted from the literature. Each point represents an H II region with radio temperatures being a weighted mean of determinations from Quireza et al. (2006) and Balser et al. (2011). Despite the reduced number of regions, the obtained relation is described by the weighted fit

$$t_e([\text{O III}]) = (0.175 \pm 0.080) + (0.792 \pm 0.081) \times t_e^* \quad (12)$$

This result differs from that established by Shaver et al. (1983), who found that the weighted average of the ratio of these temperatures is $t_e([\text{O III}])/t_e^* = 1.06 \pm 0.02$, with the result that the slope derived here is smaller than their value. Their relation was obtained from only six H II regions located close to the Sun, but we have not found other studies in the literature that can be compared with our results.

We applied the relation obtained to those regions of the sample without direct estimations of optical temperatures, but with information of radio temperature from the literature (S98, S209, and S228). Once $t_e([\text{O III}])$ was estimated for each region using Eq. 12, we calculated temperatures associated with other ions with different ionisation degrees ($t_e([\text{N II}])$ with Eq. 8 and $t_e([\text{S III}])$ with Eq. 9). Finally, we inferred chemical abundances following the same procedure as for regions with observable auroral lines (Sect. 3.3). Electron temperatures, ionic abundances, and chemical abundances derived with this method are shown in Table 7. For two regions, S98 and S288, chemical abundances

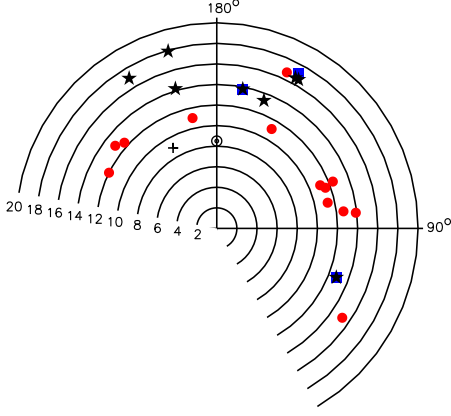


Fig. 6. Distribution of the H II regions analysed in this study projected onto the Galactic plane. The numbers close to the circles show distances to the Galactic centre in kpc. Red circles denote regions with abundances estimated with direct methods, black squares represent results from tailor-made models, and blue squares plot the abundances obtained from the $t_e - t_e^*$ relation. Regions with chemical abundances estimated with two methods are represented twice. The Sun and M 42 are also represented at $R_G=8.5$ kpc (black solar symbol) and $R_G=8.95$ kpc (black cross), respectively.

were also estimated resorting to the photoionisation models described in the previous section; as can be seen (Tables 6 and 7), both derivations are consistent within errors.

4. Discussion

4.1. Galactocentric distances of the H II regions

The study of abundance gradients in galaxies is strongly affected by the uncertainty in galactocentric distance: it can affect the slope and, therefore, the interpretation of the results. The main difficulty in establishing the parameters shown in Cols. 4 and 5 of Table 2 was to decide what Galactocentric radius of the H II regions to adopt in this work. We searched in the literature for the most accurate distances for our sample, and found several previous works which used different methods: stellar photometry, kinematical, or mixed techniques. In order to generate a self-consistent sample and to minimise the effects of inaccuracies in distances, we selected Galactic and heliocentric distances from the same catalogue for all the regions whenever possible.

Taking these considerations into account, in a first attempt, we adopted the Galactocentric distances from Caplan et al. (2000) and Quireza et al. (2006). From these works we obtained information about R_G and d_\odot for 17 H II regions (77% of the sample). Both groups of authors use the same method, deriving distances kinematically from the observed nebular recombination line local standard of rest (LSR) velocity, assuming the Brand & Blitz (1993) Galactic rotation curve and placing the Sun at a Galactocentric distance of $R_\odot=8.5$ kpc orbiting the Galactic centre at a LSR circular velocity of $\theta=220$ km s⁻¹. The two works complement each other well since they give distances for different regions or similar estimations for those regions listed in both works. Only in the case of S212 do Caplan et al. (2000) and Quireza et al. (2006) differ in the derived distances, estimating $R_G=14.8$ kpc and 16.7 kpc, respectively. We adopted the latter

Table 8. Final derived abundance gradients towards the Galactic anticentre. Linear least-squares fits weighted by abundances errors computed using all the data (three methods) and using only direct abundances are presented separately. Abundances are in units of dex and Galactocentric radius in units of kpc.

Data used	Final abundance gradients
12+log(O/H)	
All data	$(9.006 \pm 0.112) - (0.053 \pm 0.009) R_G$
Direct	$(9.113 \pm 0.139) - (0.061 \pm 0.011) R_G$
12+log(N/H)	
All data	$(8.260 \pm 0.258) - (0.080 \pm 0.019) R_G$
Direct	$(8.331 \pm 0.274) - (0.085 \pm 0.021) R_G$
log(N/O)	
All data	$-(0.478 \pm 0.086) - (0.041 \pm 0.006) R_G$
Direct	$-(0.399 \pm 0.095) - (0.047 \pm 0.007) R_G$
12+log(S/H)	
All data	$(8.162 \pm 0.088) - (0.106 \pm 0.006) R_G$
Direct	$(8.194 \pm 0.089) - (0.108 \pm 0.006) R_G$
12+log(Ar/H)	
All data	$(7.178 \pm 0.073) - (0.074 \pm 0.006) R_G$
He/H	
All data	$(0.0968 \pm 0.0259) - (0.0005 \pm 0.0019) R_G$
Direct	$(0.0982 \pm 0.0299) - (0.0007 \pm 0.0022) R_G$

because it agrees with the value proposed by Balser et al. (2011), whose estimation will be used for other regions (see below).

Five regions of our sample do not have distances estimated by Caplan et al. (2000) or Quireza et al. (2006). For these regions, we decided to use works that derive distances with the same methodology. To this end, we adopt distances derived by Fich & Silkey (1991) for S98, S266, S270, and S283 and by Balser et al. (2011) for S98. These five regions are not individually catalogued in any other study of kinematical distances. Both Fich & Silkey (1991) and Balser et al. (2011) derive kinematic distances with $R_\odot=8.5$ kpc and $\theta=220$ km s⁻¹, although Fich & Silkey (1991) use a flat rotation curve instead a curve from Brand & Blitz (1993).

Here we have thus chosen to use only these kinematic determinations of the R_G of our sources, obtaining a sample with consistent Galactocentric radius. Figure 6 shows the distribution of the 22 H II regions with derived chemical abundances projected onto the Galactic plane and plotted as function of the Galactic longitude and Galactocentric radius. They cover the anticentre range of distances from ~ 11 kpc to ~ 18 kpc.

4.2. Abundance gradients of O/H, N/H, N/O, S/H, Ar/H, and He/H towards the Galactic anticentre

From the derived abundances shown in Tables 5, 6, and 7, we can study the radial distribution of chemical abundances along the Galactic anticentre. Figures 7 through 12 show the total chemical abundances of O/H, N/H, N/O, S/H, Ar/H, and He/H, respectively, plotted against Galactocentric distances for the H II re-

Table 9. Chemical abundance gradients derived by other authors in studies with Galactic H II regions. We show the slope, $d(\log(X/H))/dR_G$, for each element X in units of dex kpc^{-1} .

Reference	Spectral range	R_G range (kpc)	O/H	N/H	S/H	N/O
Shaver et al. (1983)	radio+optical	3.5-13.7	-0.07	-0.09	-0.01	-
Simpson et al. (1995)	radio+infrared	0.1-10.2	-	-0.10	-0.07	-0.04
Vílchez & Esteban (1996) ^[a]	optical	12.4-18.0	-0.028/-0.036/-0.051	0.043/-0.009/0.002	-0.01/-0.041/-0.013	-
Afflerbach et al. (1997)	radio+infrared	0-11.4	-0.064	-0.072	-0.063	-
Rudolph et al. (1997)	radio+infrared	12.9-17.0	-	-0.111	-0.079	-
Deharveng et al. (2000) ^[b]	optical	6.5-17.7	-0.0473/-0.0395	-	-	-
Esteban et al. (2005) ^[c]	optical (RLs)	6.3-10.4	-0.044	-	-	-
Quiroza et al. (2006)	radio	0.1-16.9	-0.043	-	-	-
Rudolph et al. (2006) ^[d]	radio+infrared	0-18	-0.060/-0.041	-0.071/-0.085	-0.046/-0.042	+0.004/-0.034
Balser et al. (2011) ^[e]	radio	4.7-21.9	-0.0383/-0.0446	-	-	-
This work ^[f]	optical	11-18	-0.053/-0.061	-0.080/-0.085	-0.106/-0.108	-0.041/-0.047

^a Abundances derived from direct T_e . / Abundances derived from model-dependent methods. / All the estimations.

^b Completed sample. / Regions with direct T_e .

^c Chemical abundances derived from recombination lines (RLs) with $t^2 \neq 0$.

^d Optical data. / Far infrared data.

^e GBT sample. / Green Bank sample.

^f All data (three methods). / Only direct abundances.

gions with chemical abundances inferred in this work. To make it easier to distinguish between the three methods used to determine abundances, the regions with direct T_e are plotted as red circles, results from tailor-made models are represented with black stars, and abundances obtained from the t_e - t_e^* relation are shown as blue squares. Regions with abundances that are upper or lower limits are represented by arrows in the figures, but they have not been taken into account in any fitting.

To determine linear gradients we performed a least-squares fitting weighted by abundance uncertainties. Data from the three methods (except limit abundances) were combined into a single fit and plotted as solid lines in the figures. We also computed gradients using only abundances derived for the H II regions with direct determinations of T_e ; however, for simplicity, they are not represented in the figures. The final abundance gradients are presented in Table 8. Regions with chemical abundances derived with two methods (S98 and S228) are represented twice in the figures, but are only considered once in the performed fits; as the representative value we took the weighted mean by errors of the two methods. In addition, it is interesting to note that those abundances estimated using the electron temperature derived from the relation between optical and radio temperatures (blue squares) follow the same tendency as abundances derived with the direct method and, in general, they agree with the fits obtained.

To compare our results with other works, in Table 9 we present a summary of all the gradients obtained by different authors from H II regions in the inner and outer Galaxy in several spectral ranges. The extrapolated radial gradients obtained by Rudolph et al. (2006) with optical data are also represented in graphics as dashed lines. These come from a selection of previous works for a large range of Galactocentric distances shown here for the sake of comparison with a suggestion of flattening in the outer parts of the disc.

The radial distribution of the oxygen abundance is presented in Fig. 7 and it clearly shows a decrease with Galactocentric distance. Within the range of distances between 11 and 18

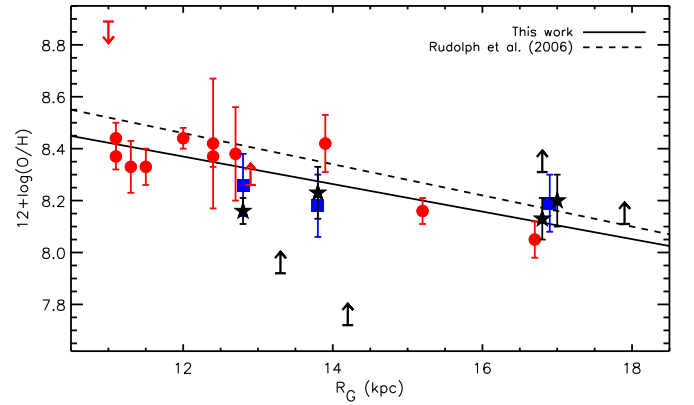


Fig. 7. Radial distribution of $12+\log(\text{O}/\text{H})$ (in dex) plotted versus Galactocentric radius (R_G in kpc). Red circles denote regions with abundances estimated with direct methods, black squares represent results from tailor-made models, and blue squares plot the abundances obtained from t_e - t_e^* relation. Regions with abundances that are upper or lower limits are represented by arrows. The solid line represents the least-squares weighted fit performed to all the data (except limits abundances), while the extrapolated gradient from Rudolph et al. (2006) is represented by a dashed line.

kpc, the maximum variation goes from $12+\log(\text{O}/\text{H})=8.44$ to $12+\log(\text{O}/\text{H})=8.05$. The results obtained by computing the fit with all the regions and by using only the abundances derived with the direct method (Table 5) are consistent, taking the associated uncertainties into account; the slope of the latter is slightly steeper.

When comparing our results with those for the inner parts of the Galaxy, we find that our slope is clearly shallower than the one obtained by Shaver et al. (1983), but in general their fits have steeper slopes than many others in the literature. In addition, our result is in very good agreement with the gradient obtained by Afflerbach et al. (1997) with infrared data. The

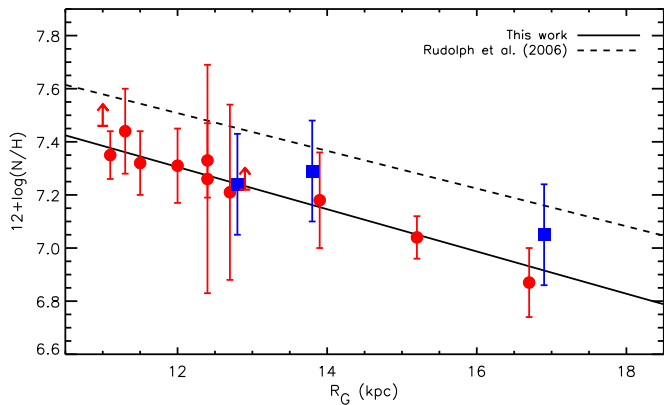


Fig. 8. Radial distribution of $12+\log(\text{N}/\text{H})$ plotted versus Galactocentric radius. Symbols and colours are as in Fig. 7.

slope obtained by Esteban et al. (2005) is smoother than ours, even though they performed the study of gradients based on recombination lines instead of collisional lines. On the other hand, our gradient is in good agreement with those performed in a wider range of distances (0 to 18 kpc) and, as can be seen in Fig. 7, our slope agrees with Rudolph et al. (2006). Gradients obtained by Deharveng et al. (2000), Quireza et al. (2006), and Balser et al. (2011) are slightly shallower than ours, but are consistent within errors. Vílchez & Esteban (1996) are the only authors who have focused their study on the outer part of the Galaxy. They provide three different oxygen gradients, and our slope agrees with the one obtained from all of their data (third option in Table 9), but not with the other fits.

Figure 8 shows the radial distribution of the final N/H abundances. The derived nitrogen abundances present values between $12+\log(\text{N}/\text{H})=7.44$ and 6.88 and their distribution shows a clear decrease with distance. Observed values follow closely the performed fit, although those derived from radio temperatures (blue squares) are slightly higher, but still in agreement within measured errors. The resulting fits, for all the regions and for direct abundances alone, are in agreement, taking the errors into account.

Within the uncertainties this result for the nitrogen gradient is not different from those found by Shaver et al. (1983), Simpson et al. (1995), Rudolph et al. (1997), Afflerbach et al. (1997), and Rudolph et al. (2006). However, our slope differs from that obtained by Vílchez & Esteban (1996) for a similar range of R_G : we do not see any clear steepening of nitrogen in the outer part of the Galaxy disc.

Figure 9 shows the behaviour of N/O versus Galactocentric distance for the studied regions. The derived values of N/O range from $\log(\text{N}/\text{O})=-0.87$ to -1.19 . In this case almost no difference exists between the slope derived from directly derived abundances and the value considering also abundances derived using model fits, since the latter have much higher associated errors and they thus have a lower weight in the fit. Our slope is consistent with the value obtained by Simpson et al. (1995) from infrared observation in the inner parts of the Galaxy, but differs from Rudolph et al. (2006) who found that N/O is nearly constant at all distances. The fit of the data shown in Fig. 9 presents a decreasing slope in N/O with Galactocentric distance, although a step function is also plausible (see next section).

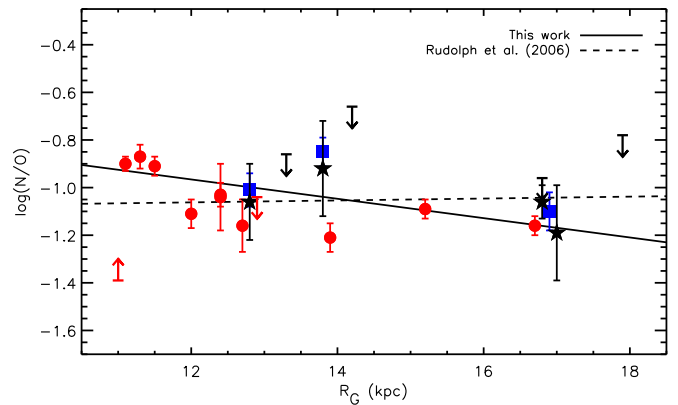


Fig. 9. Radial distribution of $\log(\text{N}/\text{O})$ plotted versus Galactocentric radius. Symbols and colours are as in Fig. 7.

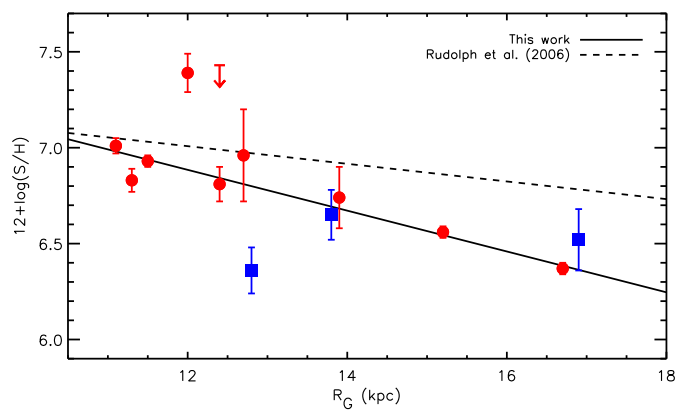


Fig. 10. Radial distribution of $12+\log(\text{S}/\text{H})$ plotted versus Galactocentric radius. Symbols and colours are as in Fig. 7.

The sulphur radial gradient is plotted in Fig. 10. The derived sulfur abundances present values between $12+\log(\text{S}/\text{H})=7.01$ and 6.37 along the range of Galactocentric distances, with the exception of the high S/H value of S311 (which has the lowest value of $t_e([\text{S III}])$) and the low estimation of S/H in S98. The distribution shows a negative radial gradient with a slope that is much steeper than those derived by other authors. This may be a consequence of the large weight of regions located at large Galactic radius whose abundances have very low errors.

In Fig. 11, we present the argon gradient along the Galactocentric anticentre. The distribution ranges from $12+\log(\text{Ar}/\text{H})=6.4$ to 5.9 , decreasing clearly with distance. In this case all the abundances represented were derived using the direct method (direct measures of electron temperature for all the regions) and we only show one fit for the gradient in Table 8. This is the first time that the distribution of argon towards the Galactic anticentre is shown. Shaver et al. (1983) derived a gradient of $d(\log(\text{Ar}/\text{H}))/dR_G=-0.06\pm 0.015$ in the inner part of the Galaxy, which is in good agreement with our slope, taking the fit uncertainties into account.

Finally, Fig. 12 shows the radial distribution of helium abundances. The derived values of He/H cluster around $\text{He}/\text{H}\sim 0.09$ no matter their Galactocentric distances. There is no obvious gradient and the least-squares fit to the data gives a slope that

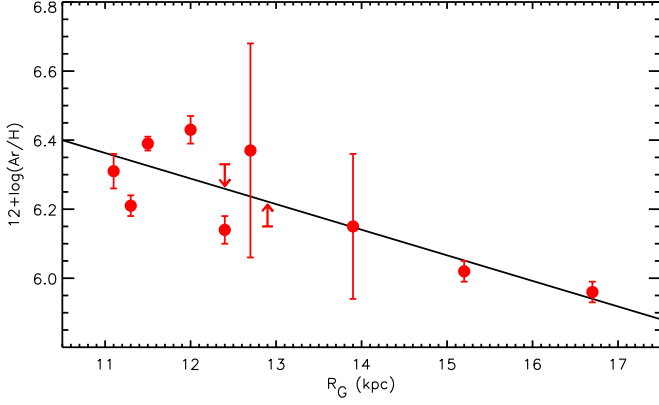


Fig. 11. Radial distribution of $12+\log(\text{Ar}/\text{H})$ plotted versus Galactocentric radius. Symbols and colours are as in Fig. 7.

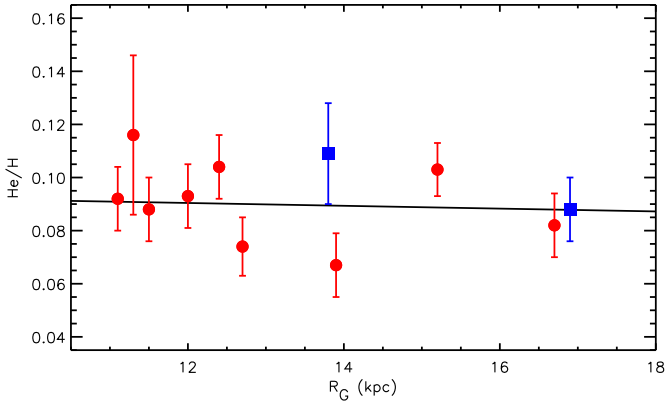


Fig. 12. Radial distribution of He/H plotted versus Galactocentric radius. Symbols and colours are as in Fig. 7.

is not significantly different from zero. Trying to compare our results with those of other authors, we find that no attempts have been made previously to estimate the total helium radial abundance gradient of the Galaxy, only the distribution of He^+/H^+ has been studied before with slopes also close to zero (Peimbert et al. 1978; Talent & Dufour 1979; Shaver et al. 1983; Deharveng et al. 2000).

4.3. Chemical composition of the outer Galaxy

The knowledge of the chemical distribution across the Galactic disc is a benchmark for models of chemical evolution. For this reason, considerable effort has been made to establish the abundance gradients in the MW by studying the distribution of many elements and many sources which all probe different epochs in the MW chemical evolution history. Figure 13 provides comparisons of our O/H abundance gradient derived from the total H II region sample towards the anticentre with many other gradients derived from studies with PNe, cepheids, B-type stars, and H II regions in a wide range of Galactic distances (0-20 kpc). The gradients adopted for the different objects are shown in Table 10 and are those provided directly by the authors. Moreover, oxygen abundances derived in the Large and Small Magellanic Clouds (Russell & Dopita 1990), Orion nebula (Tsamis et al. 2011), and the Sun (Asplund et al. 2009) are also represented in Fig. 13.

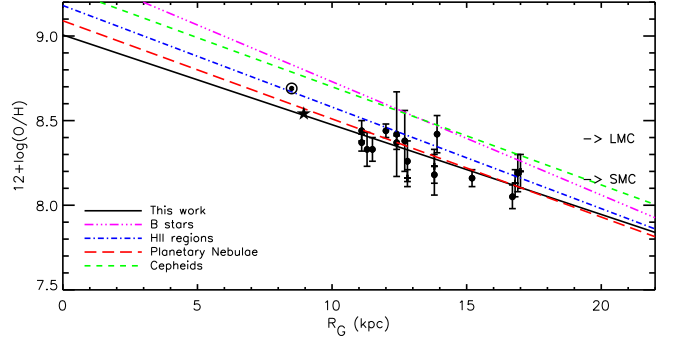


Fig. 13. Extrapolated gradients of $12+\log(\text{O}/\text{H})$ along the Galactic disc for different sources. Black circles represent all the H II regions studied in this work and the solid black line indicates the gradient obtained with them. Gradients derived from PNs (long dashed red line), H II regions (dash-dotted blue line), B-type stars (dash-dot-dotted pink line) and Cepheids (short-dashed green line) are also represented. The Sun and the Orion nebula (M42) are shown at their respective O/H abundances located at $R_G = 8.5$ kpc and $R_G = 8.95$ kpc, respectively. Horizontal arrows show chemical abundances of the Small and Large Magellanic Clouds.

B-type stars are massive young stars (<10 Myr) and their abundances trace the metallicity near their current location. Rolleston et al. (2000) studied a sample of about 80 early B-type main sequence stars located from 6 to 18 kpc. They conclude that the distribution of oxygen can be represented by a linear gradient with no evidence of a better fitting with a two-zone model. As we can see in Fig. 13 and Table 10, the results from Rolleston et al. (2000) are the most different to ours, with a much steeper slope and the largest ordinate at origin.

Planetary nebulae trace metallicity in the Galactic disc, bulge, and halo. Their ages span 1-8 Gyr and thus PNe can in principle probe metallicity with time. We compare our results with those obtained from Henry et al. (2010) who determined chemical abundances of 124 PNe extending from 0.9 to 21 kpc in Galactocentric distances. We find an agreement in slope with their gradient as we can see in Fig. 13 and Table 10. They found some evidence that the gradient beyond 10 kpc is steeper than it is inside this distance.

Cepheids are evolved stars that can be detected at large distances and are relatively young (<200 Myrs), hence they are primary tracers of metals in the Galactic disc. We compare our gradient with that obtained by the recent work of Korotin et al. (2014) and find a good agreement between the two slopes. They also found some evidence that the distribution might become flatter in the outer parts of the disc.

Galactic H II regions are the formation sites of massive OB stars and they reveal the location of current Galactic star formation. In Fig. 13 we also represent the gradient obtained by Rudolph et al. (2006), considering it as a collection of previous studies with H II regions. Their results are consistent with ours, taking the uncertainties into account.

What do we conclude from these studies? The existence of those gradients offers the opportunity to compare with models of disc evolution to understand the formation and chemical evolution of our Galaxy. All the results obtained from different sources present a negative radial gradient (although with significant differences in their slopes), thus metal abundances in

Table 10. Comparison of oxygen gradient obtained from different sources.

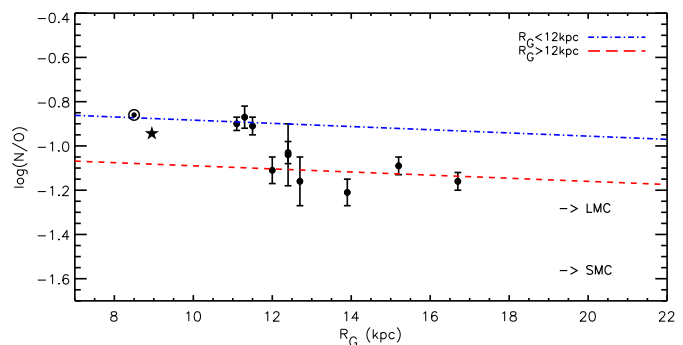
Author(s)	Object type	$d(\log(\text{O}/\text{H}))/dR_G$ (dex/kpc ⁻¹)	ΔR_G (kpc)
This work	H II regions	-0.053	11-18
Rolleston et al. (2000)	B stars	-0.067	6-18
Rudolph et al. (2006)	H II regions	-0.060	5-18
Henry et al. (2010)	PNe	-0.058	0.9-21
Korotin et al. (2014)	Cepheids	-0.058	5-18

the inner disc are higher than those in the outer disc. This result supports the Inside-Out formation scheme of the disc (Hou et al. 2000; Alibés et al. 2001; Chiappini et al. 2003). The inner part of the disc always forms first, and the outer part forms progressively later as gas with higher angular momentum settles into the equatorial plane at larger radii, causing the disc to grow outward with time. The metal abundance of the innermost part of the disc is higher because of the prior enrichment of the infalling gas before it reaches the equatorial plane, and the metal abundances of the outermost part of the disc is smaller because of the relatively long time scale for star formation and metal enrichment. Therefore, the negative gradients obtained in this work and results from other sources are consistent with Inside-Out models; the differences in slopes can be explained by the amount of material, yields, and star formation rates adopted by the model (e.g. Mollá et al. 2015).

As far as the shape of the gradient is concerned, the possibility of variations in the slope towards the outer disc is still widely debated. Several works (not represented in Fig. 13 for clarity) based on different tracers (cepheids, open clusters, PNe, and H II regions) have found evidence that the radial abundance gradient of some elements may flatten out at the outer part of the Galaxy disc (Fich & Silkey 1991; Vílchez & Esteban 1996; Maciel & Quireza 1999; Andrievsky et al. 2004; Costa et al. 2004; Luck et al. 2006; Carraro et al. 2007; Pedicelli et al. 2009; Henry et al. 2010; Andruzzi et al. 2011; Korotin et al. 2014). In addition, strong evidence for flattening at large distances of discs of other spiral galaxies has been presented in several papers (van Zee et al. 1998; Goddard et al. 2011; Werk et al. 2011; Bresolin et al. 2012).

Our sample is located towards the anticentre; in order to analyse the radial behaviour of the abundance gradient in the outermost disc, we need to make a comparison with literature gradients performed in wider radial ranges including the inner parts of the Galaxy. When doing so, our data suggest a shallower slope. Although this result does not necessarily imply a flattening of the gradient in the outer disc, what is clear is that the simple extrapolation of the inner slope towards the anticentre is not consistent with the observations.

From the theoretical point of view, several chemical evolution models have been computed to reproduce the flattening observed. However, authors suggest different physical mechanisms to explain this behaviour: lower effective yields in the outer disc than in the inner disc (Twarog et al. 1997), effective suppression of mixing processes near the corotation circle (Andrievsky et al. 2002; Luck et al. 2003; Andrievsky et al. 2004), constant density distribution of the halo stellar component in the inner 20 kpc (Cescutti et al. 2007), levelling out of the star formation efficiency about and beyond the isophotal radius (Esteban et al. 2013), etc. More information about this topic can be found in Bresolin et al. (2012), who discuss several


Fig. 14. Radial distribution of N/O plotted versus Galactocentric radius. Black points represent N/O abundances obtained with the direct method. The two lines represent the fit to data in two distances ranges: within 12 kpc from the Galactic centre (blue dot-dashed line) and farther than this limit (red dashed line), see text for details. The Orion nebula, the Sun and Magellanic Clouds are represented as in Fig. 13.

mechanisms that can be responsible for the flattening in the outermost disc of spiral galaxies.

The N/O abundance ratio is a useful indicator of the chemical age of the galaxy and how evolved the disc is. An interesting feature suggested by Fig. 9 is that our N/O gradient seems to be better represented by a step function instead of a linear fit. We compute a new double fit using only those N/O abundances derived from the direct method (Table 5) and differentiating those regions placed within 12 kpc from the centre and farther than this limit. The result for $R_G < 12$ kpc is

$$\log(\text{N}/\text{O}) = -(0.7264 \pm 1.3963) + (0.0152 \pm 0.1240) R_G,$$

while for $R_G > 12$ kpc we obtain

$$\log(\text{N}/\text{O}) = -(0.8993 \pm 0.1689) + (0.0150 \pm 0.0116) R_G.$$

Figure 14 shows the radial distribution of direct N/O abundances within the two fits performed with data at $R_G < 12$ kpc (blue dot-dashed line) and $R_G > 12$ kpc (red dashed line). As can be seen, both data sets are represented by lines with similar slopes (nearly constant) but different origins as the N/O ratio is uniform in two distance ranges. We conclude that the N/O distribution with Galactic distance for the disc can be better described by a step function rather than a linear gradient. Furthermore, with this double fit the statistical dispersion is obviously smaller than with the single fit.

From the point of view of chemical evolution, the origin of nitrogen is still a matter of important debate because it can have a primary or secondary origin. The overall picture of the chemical composition of galaxies seems to indicate that there are two main behaviours in the N/O versus O/H relationship depending on metallicity: a flat line with $\log(\text{N}/\text{O}) = -1.46$ (Garnett 1990) for the data of low-mass and irregular galaxies with $12 + \log(\text{O}/\text{H}) < 8.3$, and a strong slope for the N/O data against oxygen abundance for metal-rich regions. The first case reflects the proportion of the true primary production of nitrogen (independent of oxygen abundance), which is believed to be synthesised in massive stars. The second situation explains the existence of secondary nitrogen (proportional to oxygen abundance) processed in the CNO burning during the stellar evolution and returned into the ISM via PNe or stellar winds of massive stars (e.g. Edmunds 1990, Mollá et al. 2006).

In Fig. 15 we analyse the behaviour of nitrogen abundances (top panel) and N/O ratio (bottom panel) versus oxygen abun-

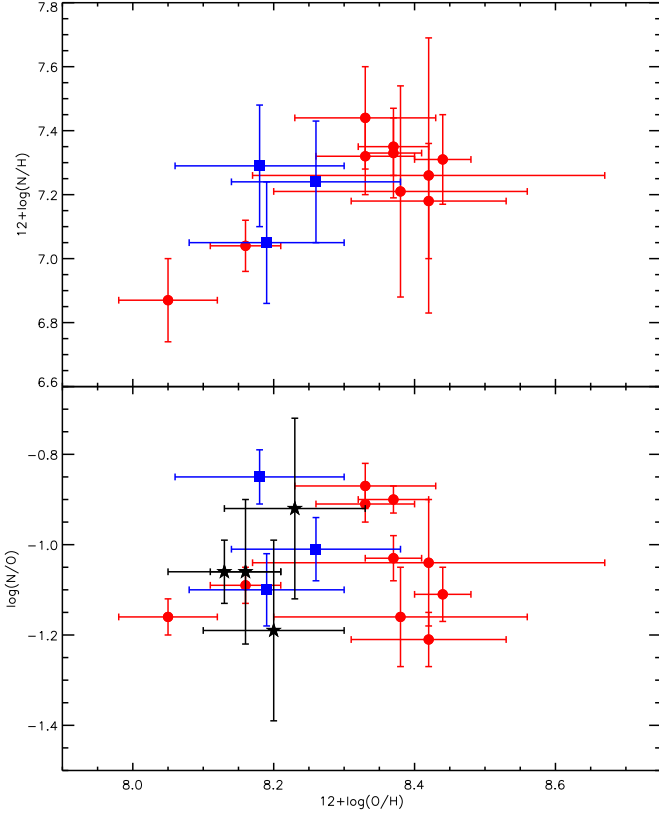


Fig. 15. Top panel: Relation between nitrogen and oxygen abundances. Bottom panel: Relative abundance, $\log(N/O)$, versus the oxygen abundance. Symbols and colours are as in Fig. 7.

dances for the regions located towards the anticentre studied in this work. As can be seen, nitrogen follows oxygen and the N/O ratio is constant with O/H, suggesting that nitrogen has a primary origin. However, our data show that in this zone $\log(N/O) > -1.46$, which is indicative of a previous enrichment by evolved intermediate mass stars (the secondary nitrogen component). In this case, the fact that N/O is constant informs us that all regions have a similar “chemical age” (understanding age in the sense of the time since the bulk of its star formation occurred). The observed N/O values and radial behaviour in the outer parts of the disc compared to the solar neighbourhood can be understood if we are witnessing a special time in the chemical evolution of the outer MW; in the Edmunds & Pagel (1978) chemical age scenario this can be a result of the increase in nitrogen abundance from intermediate-mass stars. When comparing our nitrogen distribution with the abundances in the Magellanic Clouds, it can be seen that our N/O ratio appears larger than the value for the SMC and LMC, $\log(N/O) = -1.58 \pm 0.16$ and $\log(N/O) = -1.30 \pm 0.30$, respectively (Russell & Dopita 1990), for a range in $\log(O/H)$ comparable to the abundances measured in the outer disc; this is in line with the chemical ageing scenario mentioned before for the outer disc of the MW.

5. Summary and conclusions

The abundances of heavy elements in the ISM provide a fossil record of the enrichment which has taken place due to the nucleosynthesis in successive generation stars. The study of the radial variations of metallicity across the Galactic disc is a powerful method for understanding the history of star formation and

chemical evolution of the MW. The primary focus of this paper was to give an accurate description of the radial chemical distribution towards the Galactic anticentre up to a distance of 18 kpc.

We have carried out new optical spectroscopic observations of nine H II regions located towards the Galactic anticentre using the ISIS spectrograph at the WHT. To realise a more extensive study, the sample was increased by searching for optical H II regions at $R_G > 11$ kpc in the literature. The complete sample comprised 23 H II regions extending in Galactocentric radius from 11 kpc to 18 kpc.

For 13 regions of the sample we have derived accurate electron densities from the $[S II] \lambda\lambda 6717, 6731$ line ratio and electron temperatures $t_e([O III])$, $t_e([S III])$, $t_e([N II])$, $t_e([O II])$, and $t_e([S II])$. These physical parameters have been used to determine direct total chemical abundances. We have also performed tailor-made photoionisation models to derive chemical abundances for those regions without direct estimations of temperature. In addition, by comparing radio recombination temperatures from the literature and optical temperatures from this work, we have obtained the empirical relation $t_e([O III]) = (0.175 \pm 0.080) + (0.792 \pm 0.081) \times t_e^*$. This relation has been applied to three regions without direct temperature to obtain their physical parameters and abundances.

To study the radial gradients of metallicity across the outermost part of the MW, we have performed weighted least-squares fits to the distribution of the O/H, N/H, N/O, S/H, Ar/H, and He/H abundances along the Galactocentric distances. We have concluded the following:

1. The radial distribution of oxygen abundance is fit well by a regression whose form is $12+\log(O/H) = (9.006 \pm 0.112) - (0.053 \pm 0.009)R_G$, where R_G is the Galactocentric radius in kpc. When comparing our result with gradients performed with several objects in wider radial ranges, including the inner parts of the Galaxy, we find a suggestion for a shallower slope. Our data cannot be used to confirm the flattening of the abundance gradient towards the outer disc suggested previously, but clearly show that a linear extrapolation of the inner slope is inconsistent with the observations
2. The derived gradient for N/H abundances shows a clear decrease with distance with a slope of -0.080 ± 0.019 dex kpc^{-1} . This result is in good agreement with previous works. We do not see any steepening of nitrogen in the outer part of Galaxy disc.
3. In the case of the N/O ratio, the radial distribution is better described by a step function rather than a linear gradient. The double-fit performed shows different behaviours for regions located beyond 12 kpc than for those with $R_G < 12$ kpc, but both with constant slopes. The radial behaviour in the outer parts of the disc compared to the solar neighbourhood can be understood if we are witnessing a special time in the chemical evolution of the outer MW, which can be a result of the increase in nitrogen abundance from intermediate-mass stars.
4. The fit obtained for the distribution of sulphur abundance is $12+\log(S/H) = (8.162 \pm 0.088) - (0.106 \pm 0.006)R_G$. This gradient shows a slope that is much steeper than those derived by other authors, probably reflecting the more accurate values from our data at large Galactic distances.
5. The argon gradient has been derived for the first time in regions towards the Galactic anticentre with the functional form $12+\log(Ar/H) = (7.178 \pm 0.073) - (0.074 \pm 0.006)R_G$. This

result is in good agreement with the value obtained in the inner part of the disc.

6. The total helium radial abundance gradient has been also presented here for the first time. The least-squares fit to the data gives a slope that is not significantly different from zero.

Acknowledgements. This work has been partially funded by the project AYA2013-47742-C4-1. A.M. acknowledges funding from the Spanish AYA2007-66804 and AYA2012-35330 grants. We thank D. Díaz-Fraile, A. Sota, J. Blasco, and the ESTALLIDOS collaboration for their useful comments and scientific support.

References

- Afflerbach, A., Churchwell, E., & Werner, M. W. 1997, *ApJ*, 478, 190
- Alibés, A., Labay, J., & Canal, R. 2001, *A&A*, 370, 1103
- Andreu, G., Bragaglia, A., Tosi, M., & Marconi, G. 2011, *MNRAS*, 412, 1265
- Andrievsky, S. M., Kovtyukh, V. V., Luck, R. E., et al. 2002, *A&A*, 392, 491
- Andrievsky, S. M., Luck, R. E., Martin, P., & Lépine, J. R. D. 2004, *A&A*, 413, 159
- Asplund, M., Grevesse, N., Sauval, A. J., & Scott, P. 2009, *ARA&A*, 47, 481
- Balser, D. S., Rood, R. T., Bania, T. M., & Anderson, L. D. 2011, *ApJ*, 738, 27
- Barker, T. 1980, *ApJ*, 240, 99
- Binette, L., Dopita, M. A., Dodorico, S., & Benvenuti, P. 1982, *A&A*, 115, 315
- Binette, L., Matadamas, R., Hägele, G. F., et al. 2012, *A&A*, 547, A29
- Blitz, L., Fich, M., & Stark, A. A. 1982, *ApJS*, 49, 183
- Brand, J., & Blitz, L. 1993, *A&A*, 275, 67
- Bresolin, F., Kennicutt, R. C., & Ryan-Weber, E. 2012, *ApJ*, 750, 122
- Caplan, J., Deharveng, L., Peña, M., Costero, R., & Blondel, C. 2000, *MNRAS*, 311, 317
- Carraro, G., Geisler, D., Villanova, S., Frinchaboy, P. M., & Majewski, S. R. 2007, *A&A*, 476, 217
- Cardelli, J. A., Clayton, G. C., & Mathis, J. S. 1989, *ApJ*, 345, 245
- Cescutti, G., Matteucci, F., François, P., & Chiappini, C. 2007, *A&A*, 462, 943
- Chiappini, C., Romano, D., & Matteucci, F. 2003, *MNRAS*, 339, 63
- Chini, R., & Wink, J. E. 1984, *A&A*, 139, L5
- Conti, P. S., & Leep, E. M. 1974, *ApJ*, 193, 113
- Costa, R. D. D., Uchida, M. M. M., & Maciel, W. J. 2004, *A&A*, 423, 199
- Crampton, D., & Fisher, W. A. 1974, *Publications of the Dominion Astrophysical Observatory Victoria*, 14, 283
- Crampton, D., Georgelin, Y. M., & Georgelin, Y. P. 1978, *A&A*, 66, 1
- De Robertis, M. M., Dufour, R. J., & Hunt, R. W. 1987, *JRASC*, 81, 195
- Deharveng, L., Peña, M., Caplan, J., & Costero, R. 2000, *MNRAS*, 311, 329
- Edmunds, M. G. 1990, *MNRAS*, 246, 678
- Edmunds, M. G., & Pagel, B. E. J. 1978, *MNRAS*, 185, 77P
- Esteban, C., Vilchez, J. M., Machado, A., & Edmunds, M. G. 1990, *A&A*, 227, 515
- Esteban, C., García-Rojas, J., Peimbert, M., et al. 2005, *ApJ*, 618, L95
- Esteban, C., Bresolin, F., Peimbert, M., et al. 2009, *ApJ*, 700, 654
- Esteban, C., Carigi, L., Copetti, M. V. F., et al. 2013, *MNRAS*, 433, 382
- Ferland, G. J., Porter, R. L., van Hoof, P. A. M., et al. 2013, *Rev. Mexicana Astron. Astrofis.*, 49, 137
- Fich, M., & Blitz, L. 1984, *ApJ*, 279, 125
- Fich, M., & Silkey, M. 1991, *ApJ*, 366, 107
- Garnett, D. R. 1990, *ApJ*, 363, 142
- Garnett, D. R. 1992, *AJ*, 103, 1330
- Georgelin, Y. P., & Georgelin, Y. M. 1970, *A&A*, 6, 349
- Georgelin, Y. M., Lortet-Zuckermann, M. C., & Monnet, G. 1975, *A&A*, 42, 273
- Goddard, Q. E., Bresolin, F., Kennicutt, R. C., Ryan-Weber, E. V., & Rosales-Ortega, F. F. 2011, *MNRAS*, 412, 1246
- Guesten, R., & Mezger, P. G. 1982, *Vistas in Astronomy*, 26, 159
- Hägele, G. F., Díaz, Á. I., Terlevich, E., Terlevich, R., Pérez-Montero, E., & Cardaci, M. V. 2008, *MNRAS*, 383, 209
- Hawley, S. A. 1978, *ApJ*, 224, 417
- Henry, R. B. C., Kwitter, K. B., Jaskot, A. E., et al. 2010, *ApJ*, 724, 748
- Hou, J. L., Prantzos, N., & Boissier, S. 2000, *A&A*, 362, 921
- Hunter, D. A. 1992, *ApJS*, 79, 469
- Hunter, D. A., & Massey, P. 1990, *AJ*, 99, 846
- Kennicutt, R. C., Jr., Bresolin, F., & Garnett, D. R. 2003, *ApJ*, 591, 801
- Korotin, S. A., Andrievsky, S. M., Luck, R. E., et al. 2014, *MNRAS*, 444, 3301
- Luck, R. E., Gieren, W. P., Andrievsky, S. M., et al. 2003, *A&A*, 401, 939
- Luck, R. E., Kovtyukh, V. V., & Andrievsky, S. M. 2006, *AJ*, 132, 902
- Maciel, W. J., & Koppen, J. 1994, *A&A*, 282, 436
- Maciel, W. J., & Quireza, C. 1999, *A&A*, 345, 629
- Mampaso, A. 1991, PhD Thesis, Universidad de La Laguna
- Mayor, M., & Vigroux, L. 1981, *A&A*, 98, 1
- Mesa-Delgado, A., & Esteban, C. 2010, *MNRAS*, 405, 2651
- Moffat, A. F. J., Jackson, P. D., & Fitzgerald, M. P. 1979, *A&AS*, 38, 197
- Mollá, M., Vilchez, J. M., Gavilán, M., & Díaz, A. I. 2006, *MNRAS*, 372, 1069
- Mollá, M., Cavichia, O., Gavilán, M., & Gibson, B. K. 2015, *MNRAS*, 451, 3693
- Olive, K. A., & Skillman, E. D. 2004, *ApJ*, 617, 29
- Pauldrach, A. W. A., Hoffmann, T. L., & Lennon, M. 2001, *A&A*, 375, 161
- Pedicelli, S., Bono, G., Lemasle, B., et al. 2009, *A&A*, 504, 81
- Peimbert, M. 1967, *ApJ*, 150, 825
- Peimbert, M., & Costero, R. 1969, *Boletín de los Observatorios Tonantzintla y Tacubaya*, 5, 3
- Peimbert, M., Rayo, J. F., & Torres-Peimbert, S. 1978, *ApJ*, 220, 516
- Peimbert, M., Torres-Peimbert, S., & Ruiz, M. T. 1992, *Rev. Mexicana Astron. Astrofis.*, 24, 155
- Pérez-Montero, E., & Contini, T. 2009, *MNRAS*, 398, 949
- Pérez-Montero, E., & Díaz, A. I. 2003, *MNRAS*, 346, 105
- Pérez-Montero, E., Hägele, G. F., Contini, T., & Díaz, Á. I. 2007, *MNRAS*, 381, 125
- Pérez-Montero, E., Monreal-Ibero, A., Relaño, M., et al. 2014, *A&A*, 566, AA12
- Phillipps, S., & Edmunds, M. G. 1991, *MNRAS*, 251, 84
- Porter, R. L., Ferland, G. J., Storey, P. J., & Detisch, M. J. 2013, *MNRAS*, L91
- Quireza, C., Rood, R. T., Bania, T. M., Balser, D. S., & Maciel, W. J. 2006, *ApJ*, 653, 1226
- Rodríguez, M., & Rubin, R. H. 2004, *Recycling Intergalactic and Interstellar Matter*, 217, 188
- Rohlfs, K., & Wilson, T. L. 2000, *Tools of radio astronomy / K. Rohlfs, T.L. Wilson. New York : Springer, 2000. (Astronomy and astrophysics library,ISSN0941-7834)*
- Rolleston, W. R. J., Smartt, S. J., Dufton, P. L., & Ryans, R. S. I. 2000, *A&A*, 363, 537
- Rudolph, A. L., Brand, J., de Geus, E. J., & Wouterloot, J. G. A. 1996, *ApJ*, 458, 653
- Rudolph, A. L., Simpson, J. P., Haas, M. R., Erickson, E. F., & Fich, M. 1997, *ApJ*, 489, 94
- Rudolph, A. L., Fich, M., Bell, G. R., et al. 2006, *ApJS*, 162, 346
- Russeil, D., Adami, C., & Georgelin, Y. M. 2007, *A&A*, 470, 161
- Russell, S. C., & Dopita, M. A. 1990, *ApJS*, 74, 93
- Searle, L. 1971, *ApJ*, 168, 327
- Sharpless, S. 1959, *ApJS*, 4, 257
- Shaver, P. A., McGee, R. X., Newton, L. M., Danks, A. C., & Pottasch, S. R. 1983, *MNRAS*, 204, 53
- Shaw, R. A., & Dufour, R. J. 1995, *PASP*, 107, 896
- Simpson, J. P., Colgan, S. W. J., Rubin, R. H., Erickson, E. F., & Haas, M. R. 1995, *ApJ*, 444, 721
- Stasińska, G., Morisset, C., Simón-Díaz, S., et al. 2013, *A&A*, 551, A82
- Storey, P. J., & Hummer, D. G. 1995, *MNRAS*, 272, 41
- Talent, D. L., & Dufour, R. J. 1979, *ApJ*, 233, 888
- Tsamis, Y. G., Walsh, J. R., Vilchez, J. M., & Péquignot, D. 2011, *MNRAS*, 412, 1367
- Twarog, B. A., Ashman, K. M., & Anthony-Twarog, B. J. 1997, *AJ*, 114, 2556
- van Zee, L., Salzer, J. J., Haynes, M. P., O'Donoghue, A. A., & Balonek, T. J. 1998, *AJ*, 116, 2805
- Vilchez, J. M., & Esteban, C. 1996, *MNRAS*, 280, 720
- Vilchez, J. M., & Pagel, B. E. J. 1988, *MNRAS*, 231, 257
- Werk, J. K., Putman, M. E., Meurer, G. R., & Santiago-Figueroa, N. 2011, *ApJ*, 735, 71

Table 3. Reddening corrected line intensities relative to $H\beta=1000$ of the H II regions observed with ISIS-WHT.

Line	λ (Å)	$f(\lambda)$	$I(\lambda)/I(H\beta)$												
			S83	S132	S156	S162	S207	S208	S212	S228	S270				
[O III]	3727.43	0.322	908.8 ± 87.0	4119.4 ± 393.2	3015.6 ± 244.0	2572.5 ± 85.3	4497.0 ± 331.0	3375.0 ± 270.4	2959.8 ± 204.3	3673.2 ± 311.8	2328.3 ± 114.1 †	-	-	-	
H13	3734.37	0.320	-	-	-	11.1 ± 2.0	-	-	-	-	-	-	-	-	
H12	3750.15	0.317	-	42.1 ± 8.6	37.5 ± 3.2	32.6 ± 1.8	-	-	26.8 ± 2.8 †	-	-	-	-	-	
H11	3770.63	0.313	-	51.7 ± 8.1	42.5 ± 3.8	36.6 ± 1.3	-	-	37.4 ± 4.7 †	-	-	-	-	-	
H10	3797.90	0.307	-	63.3 ± 7.3	58.3 ± 4.8	51.7 ± 1.7	-	-	39.4 ± 4.0 †	-	-	-	-	-	
He I	3819.61	0.302	-	-	7.0 ± 0.9	11.9 ± 0.8	-	-	-	-	-	-	-	-	
H9+He I	3834.48	0.299	-	86.6 ± 9.8	82.2 ± 6.4	82.8 ± 2.3	-	-	94.8 ± 9.3	-	-	-	-	-	
[Ne III]	3869.35	0.291	-	-	13.9 ± 1.5	26.3 ± 1.2	-	-	-	-	-	-	-	-	
H8+He I	3889.05	0.286	560.4 ± 64.2	269.9 ± 28.0	202.6 ± 14.6	191.2 ± 5.2	248.4 ± 31.8 †	-	274.3 ± 23.3	256.3 ± 30.5 †	-	-	-	-	
H7+[Ne III]	3968.77	0.266	227.7 ± 43.2	238.9 ± 25.5	205.5 ± 13.8	192.6 ± 4.9	206.5 ± 27.5 †	-	234.4 ± 16.4	157.5 ± 20.9 †	-	-	-	-	
He I	4026.21	0.251	-	-	18.7 ± 1.5	20.1 ± 0.8	-	-	-	-	-	-	-	-	
[S III]	4068.60	0.239	-	41.4 ± 4.6	23.6 ± 1.6	24.7 ± 0.9	-	-	11.5 ± 1.1 †	-	-	-	-	-	
[S II]	4076.35	0.236	-	23.0 ± 5.6 †	8.6 ± 0.9	8.6 ± 0.6	-	-	-	-	-	-	-	-	
H6	4101.74	0.229	310.1 ± 36.1	322.2 ± 22.9	313.1 ± 18.1	276.9 ± 5.9	352.3 ± 32.7 †	414.3 ± 50.7 †	305.7 ± 15.4	312.0 ± 28.7	-	-	-	-	
Hγ	4340.47	0.156	535.4 ± 28.6	523.7 ± 24.6	511.8 ± 20.1	478.4 ± 6.9	515.8 ± 37.9	641.1 ± 29.3 †	513.7 ± 18.1	523.6 ± 35.5	495.4 ± 39.9	-	-	-	
[O III]	4363.21	0.149	54.6 ± 6.9	-	4.3 ± 0.6	7.0 ± 0.5	-	-	22.8 ± 2.0	-	-	-	-	-	
He I	4387.93	0.141	-	-	4.6 ± 0.5 †	5.0 ± 0.2	-	-	-	-	-	-	-	-	
He I	4471.47	0.115	-	40.3 ± 3.4	38.6 ± 1.5	36.9 ± 0.7	-	-	45.1 ± 3.0	-	-	-	-	-	
[Fe III]	4658.10	0.058	-	-	5.9 ± 0.6	2.1 ± 0.3	-	-	-	-	-	-	-	-	
[Ar IV]+He I	4712.25	0.042	-	-	4.8 ± 0.3	4.4 ± 0.3	-	-	-	-	-	-	-	-	
Hβ	4861.33	0.000	1000.0 ± 10.5	1000.0 ± 5.6	1000.0 ± 0.9	1000.0 ± 5.4	1000.0 ± 10.8	1000.0 ± 24.7	1000.0 ± 5.2	1000.0 ± 11.2	1000.0 ± 20.9	-	-	-	
He I	4921.93	-0.016	-	10.8 ± 1.1	10.8 ± 0.7	11.7 ± 0.6	-	-	13.7 ± 2.2 †	-	-	-	-	-	
[O III]	4958.91	-0.026	1829.7 ± 30.9	73.4 ± 2.5	308.2 ± 2.7	453.9 ± 1.7	101.8 ± 5.7	-	661.5 ± 3.8	143.1 ± 5.3	-	-	-	-	
[O III]	5006.84	-0.038	5804.3 ± 55.0	235.3 ± 4.2	937.2 ± 9.0	1384.4 ± 4.9	307.4 ± 6.2	-	1997.0 ± 16.7	416.2 ± 8.0	-	-	-	-	
He I	5015.68	-0.040	-	16.2 ± 2.3	24.5 ± 1.0	27.0 ± 0.3	-	-	35.5 ± 4.0	-	-	-	-	-	
[Cl III]	5517.71	-0.145	-	-	4.3 ± 0.3	5.8 ± 0.2	-	-	-	-	-	-	-	-	
[Cl III]	5537.88	-0.149	-	-	4.6 ± 0.3	4.7 ± 0.3	-	-	-	-	-	-	-	-	
[N III]	5754.64	-0.185	-	14.2 ± 1.9	9.7 ± 1.1	8.4 ± 0.7	-	-	5.9 ± 0.6	-	-	-	-	-	
He I	5875.64	-0.203	141.0 ± 5.4	131.8 ± 4.9 †	123.6 ± 3.1	116.9 ± 1.2	-	-	141.6 ± 7.0 †	-	-	-	-	-	
[O I]	6300.30	-0.263	-	-	4.0 ± 0.4	14.4 ± 0.2	-	-	-	-	-	-	-	-	
[S III]	6312.10	-0.264	15.7 ± 0.9	7.5 ± 1.0	14.4 ± 0.5	16.2 ± 0.5	-	-	16.1 ± 1.4	-	-	-	-	-	
[Si II]	6347.11	-0.269	-	-	1.8 ± 0.2	2.1 ± 0.1	-	-	-	-	-	-	-	-	
[O I]	6363.78	-0.271	-	10.6 ± 0.5 †	-	5.1 ± 0.1	-	-	-	-	-	-	-	-	
[Si II]	6371.36	-0.272	-	-	-	1.2 ± 0.2	-	-	-	-	-	-	-	-	
[N III]	6548.03	-0.296	37.7 ± 2.5	383.8 ± 2.6	250.6 ± 0.2	230.7 ± 0.2	255.2 ± 4.1	290.6 ± 9.9	110.8 ± 5.3	323.7 ± 6.3	268.2 ± 5.1	-	-	-	
Hα	6562.82	-0.298	2820.0 ± 2.2	2860.0 ± 2.8	2860.0 ± 4.1	2860.0 ± 2.6	2860.0 ± 5.3	2860.0 ± 11.4	2820.0 ± 2.5	2860.0 ± 5.2	2860.0 ± 7.2	-	-	-	
[N III]	6583.41	-0.300	111.0 ± 1.6	1157.5 ± 2.3	771.4 ± 0.9	712.3 ± 0.7	745.1 ± 7.2	919.5 ± 12.1	335.0 ± 3.9	966.7 ± 5.7	813.8 ± 8.4	-	-	-	
He I	6678.15	-0.313	38.1 ± 0.8	28.0 ± 0.5	30.4 ± 0.4	29.4 ± 0.2	-	-	33.0 ± 0.5	34.4 ± 2.3	-	-	-	-	
[S III]	6716.47	-0.318	36.8 ± 0.8	394.1 ± 2.5	97.7 ± 0.6	125.2 ± 0.5	213.4 ± 6.1	502.1 ± 4.6	104.4 ± 1.6	288.9 ± 2.9	357.4 ± 7.8	-	-	-	
[S III]	6730.85	-0.320	31.0 ± 0.9	344.2 ± 2.4	115.9 ± 0.7	159.5 ± 0.6	164.0 ± 7.2	382.3 ± 5.0	85.1 ± 1.2	240.4 ± 3.3	350.7 ± 7.8	-	-	-	
He I	7065.28	-0.365	45.7 ± 0.7	18.9 ± 0.7	37.4 ± 0.7	24.3 ± 0.2	23.6 ± 1.1 †	-	19.4 ± 0.5	21.0 ± 1.3	-	-	-	-	
[Ar III]	7135.78	-0.374	116.7 ± 2.8	79.2 ± 1.9	119.4 ± 2.3	102.7 ± 0.7	72.4 ± 2.0	-	118.6 ± 2.0	107.1 ± 2.6	-	-	-	-	
C II	7231.34	-0.387	-	-	3.1 ± 0.4 †	-	-	-	-	-	-	-	-	-	

Continues.

Table 3. Continued.

Line	λ (Å)	$f(\lambda)$	$I(\lambda)/I(H\beta)$													
			S83	S132	S156	S162	S207	S208	S212	S228	S270					
He I	7281.35	-0.393	-	-	6.2 ± 0.4	-	-	-	-	-	-	-	-	-	-	-
[O II]	7319.46	-0.399	26.1 ± 1.4 †	38.3 ± 3.3 †	45.6 ± 1.2 †	42.5 ± 0.5	66.3 ± 5.4 †	124.9 ± 7.1 †	27.6 ± 1.1 †	-	-	-	-	-	-	-
[O III]	7330.21	-0.400	14.5 ± 1.5 †	31.5 ± 3.6 †	37.4 ± 1.0 †	35.3 ± 0.7	50.4 ± 4.3 †	79.8 ± 6.6 †	20.0 ± 1.0 †	-	-	-	-	-	-	-
[Ar III]	7751.10	-0.455	33.5 ± 1.5	29.8 ± 2.3	25.3 ± 1.3	27.6 ± 0.6	-	-	32.3 ± 1.9	-	-	-	-	-	-	-
P25	8323.42	-0.525	-	-	1.0 ± 0.1	-	-	-	-	-	-	-	-	-	-	-
P24	8333.78	-0.526	-	-	1.5 ± 0.1	-	-	-	-	-	-	-	-	-	-	-
P21	8374.48	-0.531	-	-	2.2 ± 0.1	-	-	-	-	-	-	-	-	-	-	-
P20	8392.40	-0.533	-	-	2.4 ± 0.2	-	-	-	-	-	-	-	-	-	-	-
P19	8413.20	-0.535	-	-	3.2 ± 0.1	-	-	-	-	-	-	-	-	-	-	-
P18	8437.95	-0.538	-	-	3.8 ± 0.1	-	-	-	-	-	-	-	-	-	-	-
[O I]	8446.00	-0.538	-	-	4.1 ± 0.1	-	-	-	-	-	-	-	-	-	-	-
P17	8467.26	-0.541	-	-	4.8 ± 0.1	-	-	-	-	-	-	-	-	-	-	-
P16	8502.48	-0.544	-	-	5.3 ± 0.1	-	-	-	-	-	-	-	-	-	-	-
P15	8545.38	-0.549	-	-	6.1 ± 0.1	-	7.3 ± 0.2	-	-	-	-	-	-	-	-	-
P14	8598.39	-0.554	7.8 ± 0.7	-	7.4 ± 0.1	-	7.7 ± 0.2	-	6.7 ± 0.5	-	-	-	-	-	-	-
P12	8750.47	-0.568	-	-	11.3 ± 0.5	-	-	-	-	-	-	-	-	-	-	-
P11	8862.79	-0.578	-	-	15.8 ± 0.5 †	-	16.6 ± 0.7	-	-	-	-	-	-	-	-	-
P10	9015.30	-0.590	18.0 ± 2.2	18.4 ± 2.7	18.4 ± 0.4	18.4 ± 0.6	-	-	17.8 ± 2.0 †	18.4 ± 1.2	-	-	-	-	-	-
[S III]	9068.60	-0.594	212.2 ± 5.3	198.0 ± 4.0	370.8 ± 1.1	420.8 ± 0.8	211.2 ± 14.5	105.8 ± 7.1	201.4 ± 12.8	145.9 ± 1.2	73.5 ± 6.1	-	-	-	-	-
P9	9229.70	-0.604	32.8 ± 1.1	32.1 ± 0.7 †	-	-	25.8 ± 2.8	-	26.8 ± 2.0	27.9 ± 0.8	-	-	-	-	-	-
[S III] ^a	9530.60	-0.618	422.8 ± 4.8	273.7 ± 16.3	557.7 ± 3.9	661.6 ± 2.0	491.8 ± 40.2	195.5 ± 18.8	468.3 ± 32.1	460.8 ± 5.2 †	192.1 ± 12.1	-	-	-	-	-
P8	9546.2	-0.618	44.4 ± 3.3 †	-	35.0 ± 0.6	-	-	-	29.7 ± 4.2	-	-	-	-	-	-	-
P7	10049	-0.624	-	-	52.9 ± 2.4	47.8 ± 1.5	-	-	41.9 ± 4.0 †	-	-	-	-	-	-	-
F(H β) ^b			5.41 ± 1.30	2.63 ± 0.78	39.49 ± 9.93	17.55 ± 1.61	23.61 ± 5.25	7.73 ± 1.12	68.26 ± 14.59	61.83 ± 15.67	27.98 ± 3.74	-	-	-	-	-
c(H β)			2.66 ± 0.10	1.36 ± 0.13	1.57 ± 0.11	0.98 ± 0.04	1.50 ± 0.10	1.41 ± 0.06	1.42 ± 0.09	1.54 ± 0.11	1.91 ± 0.06	-	-	-	-	-

NOTES:

† Lines with uncertain measures. These lines are not used in the estimation of physical parameters or chemical abundances.

(a)=Line strongly affected by a sky absorption band. Not used in analysis.

(b)= Reddening-corrected H β line fluxes in units of 10^{-13} erg cm $^{-2}$ s $^{-1}$.

Table 5. Ionic and total chemical abundances for all H II regions of the sample with direct T_e estimations.

	S83	S127	S128	S132	S156	S158	S162	S206	S212	S255	S298	S301	S311
$12+\log(\text{O}^+/\text{H}^+)$	7.30 ± 0.06	8.36 ± 0.12	8.06 ± 0.24	8.30 ± 0.11	8.23 ± 0.09	8.10 ± 0.30	8.25 ± 0.07	8.17 ± 0.12	7.88 ± 0.10	8.87	7.82 ± 0.11	8.08	8.07
$12+\log(\text{O}^{2+}/\text{H}^+)$	8.09 ± 0.06	7.59 ± 0.19	8.10 ± 0.26	7.21 ± 0.15	7.62 ± 0.05	8.14 ± 0.40	7.75 ± 0.03	8.11 ± 0.03	7.56 ± 0.04	7.47	8.22 ± 0.03	7.80	8.19
$12+\log(\text{S}^+/\text{H}^+)$	5.05 ± 0.03	5.77 ± 0.07	5.68 ± 0.14	6.43 ± 0.13	5.88 ± 0.25	5.41 ± 0.16	6.11 ± 0.05	-	5.53 ± 0.05	6.10	5.93 ± 0.06	5.83	5.93
$12+\log(\text{S}^{2+}/\text{H}^+)$	6.33 ± 0.02	6.69 ± 0.18	6.89 ± 0.26	6.60 ± 0.03	6.89 ± 0.01	7.39 ± 0.88 †	6.94 ± 0.04	-	6.29 ± 0.03	-	6.63 ± 0.10	-	7.32
$12+\log(\text{N}^+/\text{H}^+)$	6.18 ± 0.03	7.11 ± 0.08	6.89 ± 0.15	7.40 ± 0.06	7.22 ± 0.05	6.94 ± 0.17	7.23 ± 0.04	-	6.70 ± 0.06	7.45	6.78 ± 0.07	7.03	6.94
$\log(\text{N}^+/\text{O}^+)$	-1.09 ± 0.04	-1.21 ± 0.06	-1.16 ± 0.11	-0.87 ± 0.05	-0.91 ± 0.04	-1.04 ± 0.14	-0.90 ± 0.03	-	-1.16 ± 0.04	-1.39	-1.03 ± 0.05	-1.04	-1.11
$12+\log(\text{Ne}^{2+}/\text{H}^+)$	7.57 ± 0.09	-	-	-	6.33 ± 0.08	-	6.57 ± 0.04	-	-	-	7.82 ± 0.04	7.04	7.43
$12+\log(\text{Ar}^{2+}/\text{H}^+)$	5.91 ± 0.02	6.05 ± 0.21	6.32 ± 0.31	6.10 ± 0.03	6.29 ± 0.02	6.28 ± 0.47 †	6.23 ± 0.05	-	5.88 ± 0.02	-	6.09 ± 0.04	6.08	6.39
$12+\log(\text{Fe}^{2+}/\text{H}^+)$	-	-	-	-	5.70 ± 0.07	-	5.21 ± 0.07	-	-	-	-	-	-
(He ⁺ /H ⁺) 4026	-	-	-	-	0.08 ± 0.01	-	0.09 ± 0.01	-	0.05 ± 0.01	-	-	-	0.09
(He ⁺ /H ⁺) 4471	-	-	-	0.08 ± 0.01	0.08 ± 0.01	-	0.08 ± 0.01	-	0.09 ± 0.01	-	-	0.09	0.11
(He ⁺ /H ⁺) 5875	0.10 ± 0.01	0.07 ± 0.01	0.06 ± 0.01	-	0.09 ± 0.01	0.10 ± 0.02	0.08 ± 0.01	0.09 ± 0.01	-	-	0.09 ± 0.01	0.09	-
(He ⁺ /H ⁺) 6678	0.10 ± 0.01	0.07 ± 0.01	0.10 ± 0.02	0.07 ± 0.01	0.08 ± 0.01	-	0.08 ± 0.01	-	0.09 ± 0.01	-	0.10 ± 0.02	0.08	0.10
(He ⁺ /H ⁺) 7065	0.11 ± 0.01	0.05 ± 0.01	0.08 ± 0.02	0.07 ± 0.01	0.09 ± 0.01	-	0.06 ± 0.01	-	0.05 ± 0.01	-	-	0.08	0.08
(He ⁺ /H ⁺)	0.10 ± 0.01	0.06 ± 0.01	0.07 ± 0.01	0.07 ± 0.01	0.08 ± 0.01	0.10 ± 0.02	0.08 ± 0.01	0.09 ± 0.01	0.07 ± 0.01	-	0.09 ± 0.01	0.09	0.09
ICF(S ⁺ , S ²⁺)	1.60 ± 0.09	1.00 ± 0.01	1.09 ± 0.10	1.00 ± 0.01	1.01 ± 0.01	1.09 ± 0.15	1.01 ± 0.01	-	1.02 ± 0.01	-	1.26 ± 0.07	-	1.12
ICF(Ne ²⁺)	1.07 ± 0.01	-	1.15 ± 0.09	-	1.65 ± 0.16	-	1.49 ± 0.09	-	-	-	1.09 ± 0.01	1.30	1.13
ICF(Ar ²⁺)	1.28 ± 0.07	1.26 ± 0.03	1.12 ± 0.04	1.29 ± 0.01	1.24 ± 0.02	1.13 ± 0.06	1.22 ± 0.01	-	1.19 ± 0.02	-	1.12 ± 0.02	1.18	1.12
ICF(Fe ²⁺)	-	-	-	-	1.41 ± 0.04	-	1.46 ± 0.04	-	-	-	-	-	-
ICF(He ⁺)	1.03 ± 0.01	1.12 ± 0.05	1.06 ± 0.04	1.66 ± 0.36	1.10 ± 0.06	-	1.14 ± 0.02	-	1.17 ± 0.03	-	1.15 ± 0.04	-	1.04
$12+\log(\text{O}/\text{H})$	8.16 ± 0.05	8.42 ± 0.11	8.38 ± 0.18	8.33 ± 0.10	8.33 ± 0.07	8.42 ± 0.25	8.37 ± 0.05	8.44 ± 0.06	8.05 ± 0.07	<8.89	8.37 ± 0.04	>8.26	8.44 ± 0.04
$12+\log(\text{S}/\text{H})$	6.56 ± 0.03	6.74 ± 0.16	6.96 ± 0.24	6.83 ± 0.06	6.93 ± 0.03	7.43 ± 0.88 †	7.01 ± 0.04	-	6.37 ± 0.03	-	6.81 ± 0.09	-	7.39 ± 0.10
$12+\log(\text{N}/\text{H})$	7.04 ± 0.08	7.18 ± 0.18	7.21 ± 0.33	7.44 ± 0.16	7.32 ± 0.12	7.26 ± 0.43	7.35 ± 0.09	-	6.87 ± 0.13	>7.46	7.33 ± 0.14	>7.22	7.31 ± 0.14
$\log(\text{N}/\text{O})$	-1.09 ± 0.04	-1.21 ± 0.06	-1.16 ± 0.11	-0.87 ± 0.05	-0.91 ± 0.04	-1.04 ± 0.14	-0.90 ± 0.03	-	-1.16 ± 0.04	>-1.39	-1.03 ± 0.05	<-1.04	-1.11 ± 0.06
$12+\log(\text{Ne}/\text{H})$	7.60 ± 0.09	-	-	-	6.55 ± 0.09	-	6.74 ± 0.05	-	-	-	7.86 ± 0.04	>7.15	7.49 ± 0.04
$12+\log(\text{Ar}/\text{H})$	6.02 ± 0.03	6.15 ± 0.21	6.37 ± 0.31	6.21 ± 0.03	6.39 ± 0.02	6.33 ± 0.47 †	6.31 ± 0.05	-	5.96 ± 0.03	-	6.14 ± 0.04	>6.15	6.43 ± 0.04
$12+\log(\text{Fe}/\text{H})$	-	-	-	-	5.85 ± 0.07	-	5.38 ± 0.07	-	-	-	-	-	-
He/H	0.10 ± 0.01	0.07 ± 0.01	0.07 ± 0.01	0.12 ± 0.03	0.09 ± 0.01	-	0.09 ± 0.01	-	0.08 ± 0.01	-	0.10 ± 0.01	-	0.09 ± 0.01

 † Uncertain abundances derived from T_e ([S III]) with $S/N < 3$.